Astronomy & Astrophysics manuscript no. DESIRED_Te_relations
May 15, 2026
©ESO 2026

The DESIRED electron temperature relations in star-forming regions of the local Universe

M. Orte-García[1,2], C. Esteban[1,2], J. García-Rojas[1,2], J. E. Méndez-Delgado[3], K. Z. Arellano-Córdova[4], A. Z. Lugo-Aranda[5], L. Toribio San Cipriano[6], F. F. Rosales-Ortega[7], I. R. Martínez-Hernández[8], and E. Reyes-Rodríguez[1,2]

[1] Instituto de Astrofísica de Canarias, E-38205 La Laguna, Tenerife, Spain e-mail: maialen.orte@iac.es
[2] Departamento de Astrofísica, Universidad de La Laguna, E-38206 La Laguna, Tenerife, Spain
[3] Instituto de Astronomía, Universidad Nacional Autónoma de México, Apartado Postal 70-264, Coyoacán, 04510, Mexico City, Mexico.
[4] Institute for Astronomy, University of Edinburgh, Royal Observatory, Edinburgh, EH9 3HJ, United Kingdom
[5] Instituto de Astronomía, Universidad Nacional Autónoma de México, A.P. 106, Ensenada 22800, BC, México
[6] Centro de Investigaciones Energéticas, Medioambientales y Tecnológicas (CIEMAT), Madrid, Spain
[7] Instituto Nacional de Astrofísica, Óptica y Electrónica (INAOE-CONAHCyT), Luis E. Erro 1, 72840, Tonantzintla, Puebla, Mexico
[8] Departamento de Astronomía y Astrofísica, Facultad de Ciencias Espaciales, Universidad Nacional Autónoma de Honduras, Bulevar Suyapa, Tegucigalpa, M.D.C, Honduras

May 15, 2026

arXiv:2605.15048v1 [astro-ph.GA] 14 May 2026

ABSTRACT

Context. Accurate determinations of chemical abundances in H II regions and star-forming galaxies rely critically on robust measurements of the electron temperature (T_e) across different ionic species. However, when using a two- or three-zone scheme to approximate the ionisation structure, it is usually possible to measure only a single temperature diagnostic, which makes it necessary to rely on empirical or theoretical relations to infer the temperatures in the remaining zones.
Aims. We present a homogeneous observational study of electron temperature (T_e) relations between different ionic species: T_e([N II]), T_e([O II]), T_e([O III]), T_e([S II]), T_e([S III]) and T_e([Ar III]), using a sample of 699 spectra of Galactic and extragalactic H II regions and star-forming galaxies (SFGs) of the local Universe.
Methods. We use the DEep Spectra of Ionised REgions Database Extended project (DESIRED-E) that comprises more than 3000 spectra of H II regions and SFGs with direct determinations of T_e. From this database we select those spectra where it is possible to determine T_e for at least two ionic species. We recalculate the electron density (n_e) and T_e using updated atomic data and a fully consistent methodology. The resulting T_e–T_e relations were examined using orthogonal distance regression fits, their total and intrinsic dispersions quantified, and the fitted slopes compared with results from previous works and predictions from photoionisation models.
Results. Relations involving low-ionisation T_e diagnostics show large intrinsic dispersions, particularly those based on T_e([O II]) and T_e([S II]), likely due to their higher sensitivity to n_e inhomogeneities, possible recombination contributions, and observational uncertainties. Relations using T_e([N II]) exhibit systematically lower dispersions, indicating that this diagnostic provides a more reliable estimate of the low-ionisation zone temperature when only higher-ionisation diagnostics are available, despite its observational difficulty at low metallicity. Overall, the fitted slopes are broadly consistent with photoionisation model predictions, particularly for relations with low intrinsic dispersion, shuch as those involving T_e([N II]) and T_e([S III]). This work provides the most comprehensive observational characterisation to date of T_e–T_e relations in local H II regions. The empirical relations presented here offer a robust basis for estimating T_e, especially when only a single diagnostic is available.

Key words. ISM: abundances – H II regions – Galaxies: abundances – Nucleosynthesis

1. Introduction

Chemical abundance calculations in ionised nebulae are primarily limited by the precision with which electron temperature (T_e) can be inferred. T_e is usually determined from the ratio of auroral to nebular collisionally excited lines (CELs) of certain ions present in the spectra of ionised nebulae. This is because the excitation energies of the upper atomic levels that give rise to auroral lines are higher than those of nebular lines, so their intensity is much more dependent on the mean energy of the free electrons whose collisions populate those upper levels and, therefore, on T_e. Optical auroral CELs – such as [O III] λ4363 , [N II] λ5755, or [S III] λ6312, among others – are normally rather faint and difficult to measure in distant and/or low-T_e ionised nebulae. Using T_e measurements to determine ionic and, ultimately, total abundances is what we call the "direct" method (e.g. Dinerstein 1990; Berg et al. 2015). With the use of ever-larger ground- and space-based telescopes and ever-more sensitive spectrographs and detectors, the direct method can apply to an increasing number of objects, even extremely distant galaxies observed with the *James Webb Space Telescope*, JWST (e.g. Arellano-Córdova et al. 2022, 2025; Schaerer et al. 2022; Curti et al. 2023; Trump et al. 2023). [O III] λ4363 is usually the brightest auroral line observed in the optical spectra of star-forming regions. This is because O is the most abundant heavy element in cosmic objects and O^{++} is

the most common species for the ionisation conditions typical in these types of objects, especially in low-metallicity ones.

It is well known that assuming nebulae as isothermal systems is not a realistic approximation. The assumption of two different T_e values for the high and low ionisation zones has been a very common method for determining ion abundances since pioneering works such as, for example, Peimbert & Costero (1969). This is because, according to photoionisation models, in radiation-bounded ionised nebulae, and especially in high-metallicity ones, T_e grows outwards due to the combination of the hardening of the ionising spectrum with increasing photoionisation optical depth and the strong cooling produced by the fine structure lines of [O III] in the inner parts of the nebula, where O^{++} dominates (e.g Stasińska 1980). In this two-zones approximation, the two most common T_e indicators used are T_e([O III]) for the high-ionisation zone and T_e([N II]) – or T_e([O II]) – for the low-ionisation zone. Some authors also propose the use of a three-zone scheme when T_e([S III]) is available, which is considered to represent an intermediate-ionisation zone (e.g. Berg et al. 2020). The determination of T_e([S III]) requires observations in the redder part of the optical spectrum to measure the nebular [S III] $\lambda\lambda 9069, 9531$ lines which, on the other hand, are greatly affected by telluric spectral features (Noll et al. 2012).

Based on the discussion above, there is a fairly general consensus to use the two-zones approximation – or even three-zones if possible, although much less frequently – to determine abundances in star-forming regions. However, [O III] λ4363 is usually the only auroral line that is measured in most star-forming regions, especially in extragalactic H II regions and definitely in star-forming galaxies (SFGs). In these cases, the so-called T_e–T_e relations are used to estimate the T_e of the low-ionisation zone and thus be able to apply the two-zone approximation. These relations can be constructed from the results of photoionisation models, but also from observations of star-forming regions where we have determinations of the two T_e indicators involved in the particular T_e–T_e relation we intend to apply. There are also situations or groups of objects in which the T_e of the low-ionisation zone is the only one available and the T_e representative of the high-ionisation zone must be estimated using T_e–T_e relations. This is the case of small Galactic H II regions ionised by early B- or late O-type stars (Esteban & García-Rojas 2018; Arellano-Córdova et al. 2021), but also of many of the H II regions in local spiral galaxies analysed in the CHAOS project (Berg et al. 2015, 2020; Croxall et al. 2016; Rogers et al. 2021, 2022). Another situation where T_e–T_e relations must be applied to obtain the T_e representative of the high-ionisation zone is when the spectrograph does not cover the spectral region of the [O III] λ4363 line, as it happens with the Multi Unit Spectroscopic Explorer (MUSE) at the 8m Very Large telescope (VLT), where observations usually only allow determining T_e([S III]), T_e([N II]), or both (e.g. Groves et al. 2023; Brazzini et al. 2024; Rickards Vaught et al. 2024).

There are many works in the literature that address and provide T_e–T_e relations for star-forming regions, using both photoionisation models and observational data. Campbell et al. (1986) were the first to propose a relation between T_e([O II]) and T_e([O III]) based on the photoionisation models of Stasińska (1982), while Garnett (1992) used his own models to propose linear T_e–T_e relations for different T_e diagnostics. Subsequent works such as those by, for example, Pagel et al. (1992), Thuan et al. (1995), Izotov et al. (1997), Oey et al. (2000), Deharveng et al. (2000), or Méndez-Delgado et al. (2023) present relations for different T_e pairs using each of them results from different photoionisation models, such as those by Stasińska (1990), Stasińska & Schaerer (1997), Sutherland & Dopita (1993), or Vale Asari et al. (2016). Studies examining T_e–T_e relations from an observational perspective have multiplied in recent decades due to the increased sensitivity of instrumentation and the aperture of available telescopes, which are able to detect faint auroral lines in an ever-increasing number of objects. There are a large number of studies that use samples from extragalactic H II regions in nearby spiral galaxies and/or dwarf galaxies of the Local Group (e.g. Vermeij & van der Hulst 2002; Kennicutt et al. 2003; Berg et al. 2015; Croxall et al. 2016; Berg et al. 2020; Rogers et al. 2021, 2022; Zurita et al. 2021; Scholte et al. 2026) or samples including both, H II regions and SFGs (e.g. Pilyugin et al. 2006, 2009; Hägele et al. 2006; Esteban et al. 2009; Yates et al. 2020; Méndez-Delgado et al. 2023; Cataldi et al. 2025) to explore empirical T_e–T_e relations. Although many works have addressed the topic to a greater or lesser extent, none of them had as their main objective the obtaining and discussion of one or more T_e–T_e relations; they are always treated as a tool in the analysis of the chemical composition or metallicity of the particular sample of objects observed or compiled in each work. Unlike the previous cases, this paper focuses exclusively on the T_e–T_e relations. Our goal is to obtain a set of T_e values calculated homogeneously and encompassing all available indicators in the optical spectra of a broad sample of star-forming regions in the Local Universe. To achieve this, we use a careful compilation of high-quality spectra and employ a refined methodology and updated atomic datasets to perform the necessary calculations.

In this paper, we recalculate T_e values obtained from diagnostics based on six line ratios of CELs of different ions for a large sample of star-forming regions of the Local Universe, focused primarily on deep high-quality emission-line spectra of Galactic and extragalactic H II regions. With all those data we analyse the behaviour of the T_e–T_e relations that can be defined from pairs of those T_e indicators. In Sect. 2 we describe the sample of spectra taken from the literature that we have used in this work. All of them have good determinations of, at least, two T_e diagnostics. In Sect. 3, we explain how we compute the physical conditions of each spectrum: its electron density (n_e) and the different T_e values that can be obtained from the CELs measured in it. In Sect. 4, we analyse the behaviour of each T_e–T_e relation obtained for the different T_e pairs selected, showing the results of the linear fits to the relations and the dispersion of the data around the fits. We discuss the results comparing with the predictions of photoionisation models and with previous results obtained by other authors from observational data. In Sect. 5 we give some suggestions on the application of the T_e–T_e relations obtained. Finally, in Sect. 6 we summarise our main conclusions.

2. Description of the sample

In this study we make use of the DEep Spectra of Ionised REgions Database (DESIRED; Méndez-Delgado et al. 2023) Extended project (DESIRED-E; Méndez-Delgado et al. 2024b). DESIRED-E is a compilation of high-quality published spectra of ionised nebulae – mainly extragalactic H II regions, SFGs, and Galactic H II regions, planetary nebulae and ring nebulae around evolved massive stars – that feature at least one T_e determination based on the following auroral to nebular intensity ratios of CELs: [O III] $\lambda 4363/\lambda 5007$, [N II] $\lambda 5755/\lambda 6584$, and/or [S III] $\lambda 6312/\lambda 9069$. For each spectrum included in DESIRED-E, we collect the extinction-corrected line intensity ratios and their associated uncertainties directly from the source papers and perform a homogeneous analysis. We only consider emission lines with observational errors less than 40%. Since DESIRED-E is frequently expanded with new spectra, the sample used in this

work corresponds to its state as of January 9, 2025, and contains 3154 spectra.

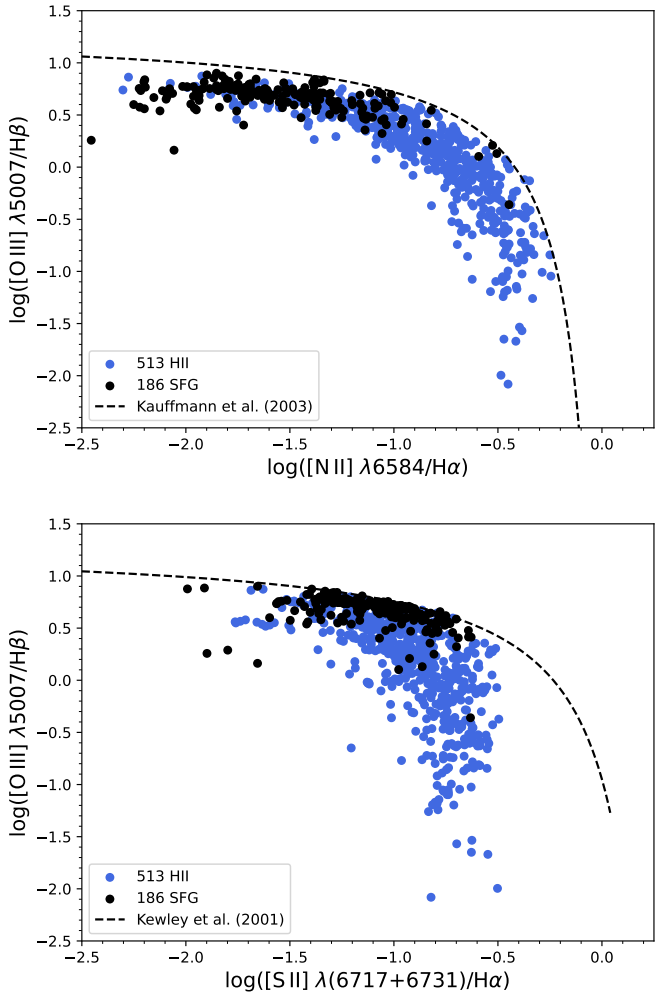


Fig. 1. Diagrams showing log([O III]λ5007/Hβ) versus log([N II]λ6584/Hα) (BPT, top) and log([O III]λ5007/Hβ) versus log([S II]$\lambda\lambda$6716 + 31/Hα) (bottom) of the sample of spectra of Galactic and extragalactic H II regions (blue dots) and star-forming galaxies (SFGs) (black squares) compiled in DESIRED-E used in this study. The dashed lines in both diagrams represent the empirical relations that have been used to distinguish between star-forming regions and active galactic nuclei (AGNs): that by Kauffmann et al. (2003) in the top diagram and Kewley et al. (2001) in the bottom one.

The aim of the present work is to explore the T_e–T_e relations in star-forming regions of the local Universe, so we limit the sample to spectra of Galactic and extragalactic H II regions and SFGs of DESIRED-E. To do this, we first filtered the sample by selecting only those spectra whose combinations of the line ratios [O III] λ5007/Hβ, [N II] λ6584/Hα, and [S II] $\lambda\lambda$6716 + 31/Hα, are consistent with pure photoionisation, as expected for star-forming regions. In the top panel of Fig. 1 we show the diagnostic diagram representing [O III] λ5007/Hβ versus [N II] λ6584/Hα, commonly known as Baldwin-Phillips-Terlevich (BPT) diagram (Baldwin et al. 1981). The selected spectra of H II regions (blue dots) and SFGs (black dots) are those located below of the Kauffmann et al. (2003) line, that is used to distinguish between star-forming regions and active galactic nuclei (AGNs). In the bottom panel of Fig. 1 we show the [O III] λ5007/Hβ versus [S II] $\lambda\lambda$6716 + 31/Hα diagnostic diagram, originally proposed by Veilleux & Osterbrock (1987). In this second diagram, we use the line proposed by Kewley et al. (2001) to separate star-forming regions from AGNs. We use both diagrams and not only the [O III] λ5007/Hβ versus [N II] λ6584/Hα one – which is the most commonly used – to ensure that at least lines of two low-ionisation species are well measured. This is especially important for metal-poor SFGs, whose high-ionisation degree can make it difficult to detect such lines in objects with low surface brightness.

The second filter applied when selecting the spectra is that, from the lines reported in the reference of each spectrum, T_e can be calculated with at least two diagnostics of the six available in the optical range: T_e([N II] λ5755/λ6584), T_e([O II] $\lambda\lambda$7319+20+30+31/$\lambda\lambda$3726+29), T_e([O III] λ4363/λ5007), T_e([S II] $\lambda\lambda$4069+76/$\lambda\lambda$6716+31), T_e([S III] λ6312/λ9069), and T_e([Ar III] λ5192/λ7135). This filter was applied to exclude excessively high T_e values due to incorrect identification of a given auroral line. To ensure that, we excluded T_e values above 20,000 K. This is a reasonable maximum value, taking into account theoretical prescriptions and the values typically observed in local metal-poor SFGs (e.g. Aller et al. 1999; Pérez-Montero & Díaz 2003; Izotov et al. 2006; Hägele et al. 2008).

The total number of DESIRED-E spectra that fulfill all our requirements is 699, of them 513 (73.4%) correspond to H II regions and 186 (26.6%) to SFGs. All these spectra have direct determinations of the total O abundance, the proxy of metallicity in ionised nebulae studies. The range of 12+log(O/H) covered by our objects goes from 7.12 to 8.92. In Table A.1 we list the 699 spectra included in the present study, indicating their object name, whether they correspond to H II regions or SFGs and the reference of their published spectra.

3. Electron density and temperature determinations

We use *PyNeb 1.1.18* (Luridiana et al. 2015; Morisset et al. 2020) with the H I effective recombination coefficients from Storey & Hummer (1995) and the atomic dataset for the N, O, S, Cl, Ar and Fe ions presented in Table 1 to determine n_e and T_e for each individual spectrum.

3.1. Electron densities

The procedure for calculating n_e and T_e of the sample objects begins using the *getCrossTemDen* routine of *PyNeb* with line intensity ratios sensitive to those quantities. The routine cross-correlates the n_e-sensitive diagnostics [O II] λ3726/λ3729, [S II] λ6731/λ6716, [Cl III] λ5538/λ5518, [Ar IV] λ4740/λ4711, and [Fe III] λ4658/λ4702 with the T_e-sensitive ones [N II] λ5755/λ6584, [O II] $\lambda\lambda$7319 + 20 + 30 + 31/$\lambda\lambda$3726 + 29, [O III] λ4363/λ5007, [S II] $\lambda\lambda$4069 + 76/$\lambda\lambda$6716 + 31, [S III] λ6312/λ9069, and [Ar III] λ5192/λ7135 using a Monte Carlo experiment of 100 iterations to propagate uncertainties in line intensities. The number of iterations was chosen as a good compromise between calculation time and convergence of the result. After each convergence, we obtain a set of n_e and T_e values for each diagnostic along with their associated uncertainties for each individual point of the experiment. The n_e value adopted for each diagnostic corresponds to the mean of the 100 individual points weighted by the inverse square of the error.

Table 1. References for atomic data used for collisionally excited lines.

Ion	Transition probabilities	Collision strengths
N^+	Froese Fischer & Tachiev (2004a)	Tayal (2004)
O^+	Froese Fischer & Tachiev (2004b)	Kisielius et al. (2009)
O^{2+}	Wiese et al. (1996), Storey & Zeippen (2000)	Storey et al. (2014)
S^+	Irimia & Froese Fischer (2005)	Tayal & Zatsarinny (2010)
S^{2+}	Froese Fischer et al. (2006)	Grieve et al. (2014)
Cl^{2+}	Fritzsche et al. (1999)	Butler & Zeippen (1989)
Ar^{2+}	Mendoza (1983), Kaufman & Sugar (1986)	Galavis et al. (1995)
Ar^{3+}	Mendoza & Zeippen (1982)	Ramsbottom & Bell (1997)
Fe^{2+}	Deb & Hibbert (2009), Mendoza et al. (2023)	Zhang (1996), Mendoza et al. (2023)

After obtaining the mean value of each n_e diagnostic, we apply the criteria proposed by Méndez-Delgado et al. (2023) to settle a mean n_e representative of each spectrum:

- If n_e([S II]) < 100 cm^{-3}, we adopt n_e= 100±100 cm^{-3}.
- If 100 cm^{-3} ≤ n_e([S II]) < 1000 cm^{-3}, we adopt the average of n_e([S II]) and n_e([O II]).
- If n_e([S II]) ≥ 1000 cm^{-3}, we adopt the average of n_e([S II]), n_e([O II]), n_e([Cl III]), n_e([Fe III]), and n_e([Ar IV]).
- In cases where a value of n_e is not reported or could not be calculated from the data of the source references, we adopt n_e=100±100 cm^{-3}.

The final adopted values of n_e for each spectrum used are given in Table A.2.

3.2. Electron temperatures

We calculate six T_e diagnostics: T_e([N II]), T_e([O II]), T_e([O III]), T_e([S II]), T_e([S III]), and T_e([Ar III]), using the *getTemDen* routine of *PyNeb* and the adopted representative n_e of each spectrum. We also use a Monte Carlo experiment of 100 iterations to propagate uncertainties in n_e and line intensities ratios involved in the T_e diagnostics. To ensure a good determination of T_e for each diagnostic and object, we verify that the flux of the pairs of nebular lines coming from the same upper atomic level used (e.g., [O III] $\lambda\lambda$5007, 4959, [S III] $\lambda\lambda$9531, 9069, [N II] $\lambda\lambda$6584, 6548) fit with their theoretical predictions (3.00, 2,47, 3.05, respectively; e.g. Storey & Zeippen 2000). We discard any diagnostic when the observed nebular line intensity ratios differ by more than 20% from the theoretical values. The [S III] $\lambda\lambda$9531, 9069 line ratio tends to differ from the theoretical one due to contamination of telluric absorption bands (see Méndez-Delgado et al. 2024a, for a discussion about this issue). There are a few objects where only one of the lines of the aforementioned pairs of nebular lines is reported. In these cases, we consider the single nebular line observed in the calculation, assuming that the T_e([S III]) value thus obtained is valid. The T_e values of the different diagnostics obtained for each spectrum are given in Table A.2. Histograms of values of the different T_e indicators used in this paper separated by group of objects (H II regions and SFGs) are shown in Fig. B.1. The median values of each T_e indicator – T_e([N II]), T_e([O II]), T_e([O III]), T_e([S II]), T_e([S III]), and T_e([Ar III]) – separated for H II regions and SFGs are given in Table B.1.

4. The T_e-T_e relations

In this section, we present and discuss the T_e–T_e relations obtained from our selected sample of DESIRED-E spectra of H II regions and SFGs that satisfy the selection criteria described in Sect. 2. Depending on the ionisation potential of the ions involved, we can distinguish T_e diagnostics of different ionisation zones within the nebula. T_e([N II]), T_e([O II]), and T_e([S II]) are commonly considered T_e indicators of the low-ionisation zone, which corresponds, in principle, to the outermost parts in radiation-bounded nebulae. On the other hand, T_e([S III]) is usually assumed as representative of the intermediate-ionisation zone, while T_e([O III]) is considered indicative of the innermost high-ionisation zone of a typical star-forming region (e.g. Berg et al. 2020). A particular case is that of T_e[Ar III] – of which we have only a few dozen determinations in DESIRED-E – which, due to the ionisation potential range where we can find Ar^{++} ions, would correspond to a zone overlapping with the S^{++} and O^{++} ones (Méndez-Delgado et al. 2023).

With six temperature diagnostics available, many T_e–T_e relations can be explored. However, we limit our analysis to those that have been most extensively studied in the literature or are of particular interest, either due to the ions involved or due to possible effects or circumstances that may affect one of the T_e diagnostics involved. In this section, we divide the analysis into three subsections. In the first, we examine the relations between the three T_e diagnostics for the low-ionisation zone. In the second and third subsections, we present and discuss T_e–T_e relations involving T_e([S III]) and T_e([O III]) on the x-axis, respectively.

For each particular T_e–T_e relation, we calculate a linear fit to analyse the correlation between both T_e diagnostics involved and compare it with the results of previous studies. Following the suggestion of Hogg et al. (2010), we use orthogonal distance regression (ODR) technique for the linear fits. This method is especially indicated when both variables are subject to error and their uncertainties are comparable. We note that the T_e – T_e relations available in the literature have been derived using a variety of fitting techniques. For instance, while we employ an ODR method, other works have used empirical model fits (e.g., Garnett 1992), standard least-squares polynomials (e.g., Méndez-Delgado et al. 2023), or a hierarchical Bayesian approach like `linmix` (e.g., Zurita et al. 2021; Rickards Vaught et al. 2024). The choice of regression can influence the final slope values. However, as we noted before, we consider the ODR method the most appropriate for this analysis, as it treats uncertainties in both variables symmetrically. We caution that some systematic differences between the slopes reported here and those in previous studies may be driven, in part, by differences in statistical treatment rather than by purely physical variations. An important advantage of the applied ODR is that it provides an invertible linear fit, i.e. the slope of the fit to the T_e(Y)–T_e(X) relation is just the reciprocal value of the T_e(X)–T_e(Y) one.

To obtain the values of the slope and intercept, we perform a Monte Carlo simulation with 10,000 iterations of the fit, using the implementation provided in the `scipy.ODR` module of SciPy. The final values and uncertainties are estimated as the median and standard deviation of the resulting distributions, respectively. To evaluate the strength and the statistical significance of the correlation between the two diagnostics used in each T_e–T_e relation we calculate the Pearson correlation coefficient, r, and the p-value[1] of each fit. In addition, we calculate the total and intrinsic dispersion of the observational points around the linear fit, σ_{tot} and σ_{int}, respectively (Rogers et al. 2021). We calculate σ_{tot} as the standard deviation of the vertical residuals, corrected for degrees of freedom. We then estimate the projected uncertainty in the dependent variable and, with this, construct a reduced χ^2 that includes an additional dispersion σ_{int}. This σ_{int} is defined as the minimum amount that makes the reduced $\chi^2 = 1$. Thus, σ_{tot} measures the actual dispersion of the residuals around the fitted relation, while σ_{int} reflects the extra physical dispersion not attributable to measurement errors, both in the y-axis. The parameters of the ODR linear fits of the T_e–T_e relations – as well as the total number of data points, the T_e range they cover on the x-axis, σ_{tot} and σ_{int} – are presented and discussed in the following subsections and included in Table 2. By providing invertible linear fits, we also calculate the corresponding σ_{tot} and σ_{int} of the T_e indicator that lies on the x-axis of a given T_e–T_e relation, calculated from the inverse ODR fit; these values are given in brackets in the last two columns of Table 2.

It is clear that an intrinsic source of scatter in the T_e–T_e relations obtained in this work is whether the nebulae are radiation-bounded or not —a characteristic that can hardly be verified for the objects in the sample. In principle, radiation-bounded nebulae should develop an ionisation stratification that would also be reflected in an internal temperature gradient. The truncation of this structure in a density-bounded nebula will alter the proportion between the different T_e diagnostics, primarily affecting relations involving T_e diagnostics of the low- and high-ionisation zones. Furthermore, the truncation of the nebular structure implies a lower fraction of low-ionisation ions, which are typically more efficient at nebular cooling under the standard physical conditions of photoionised nebulae; this will also affect their nominal T_e values.

In Méndez-Delgado et al. (2023), we presented initial results on T_e–T_e relations based on the initial version of DESIRED, limited to 190 nebular spectra. The present work represents a significant increase in the number of spectra and a considerable advance over Méndez-Delgado et al. (2023). While that study laid important groundwork, our extended sample (DESIRED-E) goes beyond a simple numerical increase; it introduces a population of high-temperature star-forming galaxies that was previously underrepresented. This inclusion has resulted in T_e–T_e relations that, in some cases, differ significantly from those of the 2023 study, especially in the high-excitation regime. Therefore, the broader coverage of physical conditions in DESIRED-E provides a more universal calibration than that offered by Méndez-Delgado et al. (2023).

Before describing our results on the T_e–T_e relations, we must remember that our study is based on a large compilation of heterogeneous data from the literature. From the papers used, we obtained the line ratios as well as their associated errors. As is well known, the criteria for estimating errors can differ significantly from one study to another, so the same line ratio could have a different nominal error in different studies. This makes it difficult, for example, to conduct a comparative study of the effect that different error values in the intensity of auroral lines might have on the T_e–T_e relations. Furthermore, the treatment of errors in flux calibration and reddening corrections is often different in different works and may introduce correlations between different temperature measurements of the spectral lines. However, since, as mentioned, our database is a meta-analysis of heterogeneous bibliographic sources, the raw calibration data and the covariance matrices necessary to quantify these correlations are not available. While these systematic effects may contribute to the observed dispersion in our relationships, the use of a large and diverse sample of objects might help to average out the calibration biases specific to each study.

4.1. Relations involving diagnostics of the low-ionisation zone

The three T_e diagnostics of the low-ionisation zone that can be derived from the optical spectra compiled in DESIRED-E are T_e([N II]), T_e([O II]), and T_e([S II]). In our sample, T_e([N II]) can be determined for 371 spectra (350 H II regions and 21 SFGs). For T_e([O II]), there are 558 spectra (435 H II regions and 123 SFGs), and for T_e([S II]), 487 spectra (361 H II regions and 126 SFGs). The comparison of the numbers corresponding to H II regions and SFGs, clearly indicates the difficulty of detecting and measuring auroral lines from low-ionisation species in SFGs, which are generally of low metallicity and therefore show a high degree of ionisation. The difficulty is especially pronounced in the case of [N II] λ5755 because metal-poor SFGs almost invariantly show a lower N/O ratio, making that line extremely weak in such objects.

Photoionisation models predict that the three T_e diagnostics representative of the low-ionisation zone follow the relation $T_e([N\,II]) \approx T_e([O\,II]) \approx T_e([S\,II])$ (Campbell et al. 1986; Garnett 1992; Pagel et al. 1992; Thuan et al. 1995; Izotov et al. 2007; Méndez-Delgado et al. 2023). However, this behaviour is not always found consistently recovered in the T_e–T_e distributions based on observational data, as we will see below.

In the top panel of Fig. 2 we show the T_e([O II])–T_e([N II]) relation obtained for 316 DESIRED-E spectra (303 H II regions and 13 SFGs) and the ODR linear fit to the data points is:

$$T_e([O\,II]) = (1.269 \pm 0.039) \times T_e([N\,II]) - (1620 \pm 320)\ \mathrm{K}. \quad (1)$$

The fit parameters given in Table 2 indicate that the correlation is clear but moderate ($r = 0.59$) and statistically significant attending to its extremely small p-value.[2] As it is shown in Table 2, the $\sigma_{tot}(T_e([O\,II]))$ of the observational data about the linear fit is 1940 K and the $\sigma_{int}(T_e([O\,II]))$ is 1160 K. The total and intrinsic dispersions in T_e([N II]) are $\sigma_{tot}(T_e([N\,II])) = 1530$ K and $\sigma_{int}(T_e([N\,II])) = 920$ K, respectively. The slope of the linear fit to T_e([O II])–T_e([N II]) is greater than one and therefore away from the predictions of the photoionisation models. Other fits of observational data of this relation or its inverse from the literature give larger values of the slope – of about 2.0 – as those by Rogers et al. (2021, 132 H II regions), Zurita et al. (2021, 196 H II regions) or Rickards Vaught et al. (2024, 132 H II regions),

[1] A value of $p > 0.05$ indicates that the null hypothesis is plausible, i.e. there is not significant linear fit between the variables. On the other hand, when $p \leq 0.05$ it can be said that there is a significant correlation between both variables.

[2] The p-values we found in all the temperature relationships studied in this work are extremely low – between 4.9×10^{-49} to 6.2×10^{-15}, indicating that all of them are statistically significant. We do not refer to the value of this parameter again in the rest of the T_e–T_e relations, to avoid repetition.

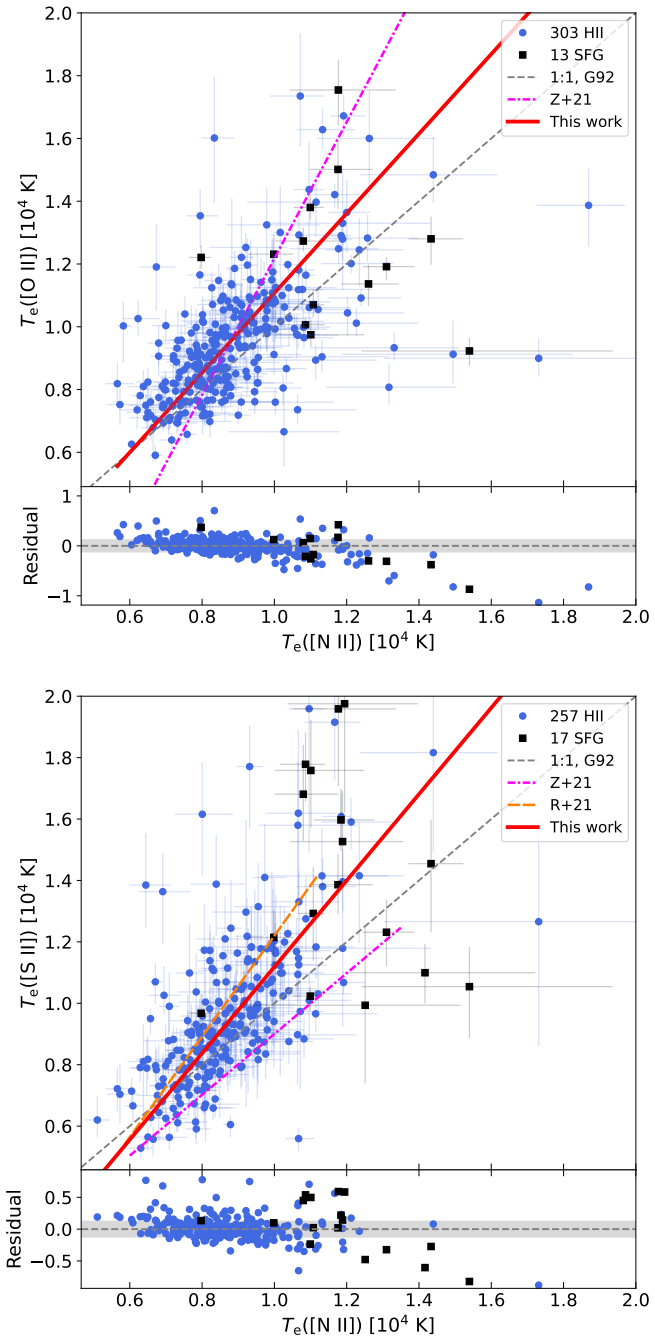


Fig. 2. T_e([O II])–T_e([N II]) (top) and T_e([S II])–T_e([N II]) (bottom) relations obtained for our DESIRED-E sample. In both panels, blue dots correspond to H II regions and black squares to SFGs, while the red continuous lines represent the ODR linear fits to the data. The grey dashed line shows the 1:1 relation that coincides with the approximate predictions of photoionisation models by Garnett (1992), and the magenta dashed line represents the linear fit obtained by Zurita et al. (2021). In the bottom panel, the orange dashed line represents the fit obtained by Rogers et al. (2021) . The fits obtained from the literature are only shown covering the T_e range from the corresponding observations on each reference. The rectangular inset below each plot shows the vertical residuals to the ODR linear fit in units of 10^4 K, with the grey band showing the total dispersion (σ_{tot}) of the data around the fit.

but also smaller – about 1.0 – as in Berg et al. (2020, 115 H II regions) or Scholte et al. (2026, 290 SFGs). In the inset at the bottom of each panel in Fig 2 (as well as in figs. 3 through 6) we include the residuals to the linear ODR fit along with a grey band indicating its corresponding σ_{tot} value. In the inset it is clear that T_e([N II]) > T_e([O II]) when T_e([N II]) > 12,000 K. The residuals shown in the insets of Figures 2–6 are defined as the vertical difference between the observed and predicted values, $\Delta T_e = T_e(\text{obs}) - T_e(\text{fit})$. It is important to note that while the fits are calculated using an ODR technique (which minimizes the perpendicular distance to the regression line), the residuals are presented as linear offsets in the ordinate in units of 10^4 K. This approach allows for a direct assessment of the uncertainty introduced when one temperature diagnostic is used to estimate another.

In the bottom panel of Fig. 2 we show the T_e([S II])–T_e([N II]) relation obtained from 274 DESIRED-E spectra (257 H II regions and 17 SFGs). The corresponding ODR linear fit to these data points is:

$$T_e([\text{S II}]) = (1.406 \pm 0.060) \times T_e([\text{N II}]) - (2880 \pm 480)\ \text{K}. \quad (2)$$

The Pearson coefficient of this fit is $r = 0.65$, indicating that the correlation is moderate-strong. For T_e([S II]), the total and intrinsic dispersions are 2140 K and 1280 K; and 1520 K and 910 K for T_e([N II]), respectively. Previous works give different values of the slope of the linear fit to the T_e([S II])–T_e([N II]) relation. From spectra of extragalactic H II regions, Rogers et al. (2021) obtain a value of 1.64 from 123 objects; Zurita et al. (2021) give a slope of 0.99 from a compilation of 160 H II regions and Rickards Vaught et al. (2024), using 189 objects, obtain a value of 0.85, the lowest slope of all determinations available. Finally, Scholte et al. (2026) obtain 1.02 from a sample of 87 SFGs.

The resulting T_e([S II])–T_e([O II]) relation obtained from our 394 spectra (314 H II regions and 80 SFGs) is presented in Fig. 3. This relation includes significantly more spectra of SFGs than the two previous ones that involve T_e([N II]). This is due to the paucity of measurements of the [N II]λ5755 line, especially faint at the low metallicities common in SFGs. The ODR linear fit to the data points shown in the figure is:

$$T_e([\text{S II}]) = (1.001 \pm 0.044) \times T_e([\text{O II}]) - (400 \pm 380)\ \text{K}. \quad (3)$$

Considering its Pearson coefficient, this linear fit indicates a moderate-strong correlation ($r = 0.64$). As we see in Eq. 3, the slope of the linear fit is entirely consistent with unity within the errors. However, the fit line shows a slight offset from the 1:1 line; T_e([O II]) systematically tends to be about 400 K higher than T_e([S II]). A very similar slope was obtained by Méndez-Delgado et al. (2023) for a much limited sample of 39 spectra and using the same methodology. However, our fit differs significantly from that obtained by Zurita et al. (2021) from a compilation of data for 175 extragalactic H II regions, who find a slope of 0.66. Scholte et al. (2026) obtain an intermediate value of 0.79, based on a sample of 365 SFGs. The total and intrinsic dispersions of the data about our linear fit are larger than those of the T_e–T_e relations discussed so far, 2430 K and 1740 K, respectively. Coincidentally, the same values for T_e([S II]) and T_e([O II]), being σ_{int} especially larger in this case with respect to the other T_e–T_e relations discussed in this subsection.

The comparison of Figs. 2 and 3 and the parameters of the linear fits given in Table 2 indicate that, while the T_e([O II])–T_e([N II]) and T_e([S II])–T_e([N II]) relations show a slope greater than one and very similar to each other, the T_e([S II])–T_e([O II]) one shows a slope consistent with unity. This is exactly the same trend reported by Méndez-Delgado et al. (2023) for a much smaller subsample – between 30 and 39 spectra – of the objects presented in this work. T_e([O II]) and T_e([S II]) tend to be higher

Table 2. Parameters of the ODR linear fits to T_e–T_e relations. Values of σ in parenthesis correspond to the inverse relation (see third paragraph of Sect. 4)

T_e–T_e	No.	T_e range (K)	Slope	Intercept (K)	r	σ_{tot} (K)	σ_{int} (K)
Relations involving diagnostics of the low-ionisation zone							
T_e([O II])–T_e([N II])	316	5660–18690	1.269 ± 0.039	−1620 ± 320	0.59	1940 (1530)	1160 (920)
T_e([S II])–T_e([N II])	274	5100–17310	1.406 ± 0.060	−2880 ± 480	0.65	2140 (1520)	1280 (910)
T_e([S II])–T_e([O II])	394	5910–18770	1.001 ± 0.044	−400 ± 380	0.64	2430 (2430)	1740 (1740)
Relations involving T_e([S III])							
T_e([S II])–T_e([S III])	257	5420–19850	0.705 ± 0.025	2760 ± 210	0.63	2090 (2970)	1410 (2010)
T_e([N II])–T_e([S III])	214	4930–16000	0.807 ± 0.022	1890 ± 180	0.75	1240 (1540)	650 (800)
T_e([O II])–T_e([S III])	303	4930–19850	0.812 ± 0.020	2390 ± 170	0.68	1770 (2140)	1480 (1800)
Relations involving T_e([O III])							
T_e([O II])–T_e([O III])	380	7320–19860	0.523 ± 0.017	5120 ± 170	0.63	1830 (3500)	1440 (2770)
T_e([N II])–T_e([O III])	204	7290–15730	0.763 ± 0.032	2530 ± 280	0.70	1360 (1780)	790 (1040)
T_e([S III])–T_e([O III])	224	7320–19540	0.953 ± 0.015	580 ± 150	0.79	1510 (1580)	1280 (1340)
T_e([Ar III])–T_e([O III])	32	7780–15600	0.911 ± 0.069	540 ± 610	0.93	890 (970)	160 (180)

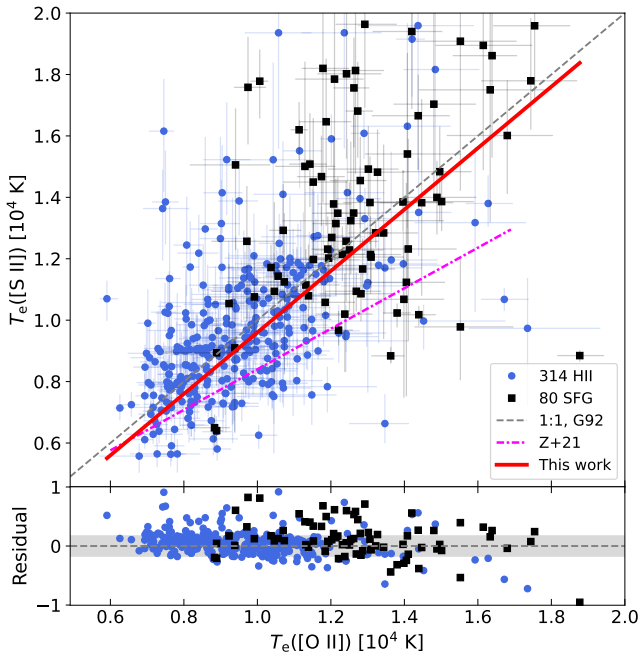


Fig. 3. Same as the upper panel of Fig. 2 but for the T_e([S II])–T_e([O II]) relation.

than T_e([N II]) in most of the range of variation of T_e([N II]), with a difference that increases toward higher T_e([N II]), a trend that has also been reported in previous studies (Pilyugin et al. 2009; Bresolin et al. 2009b; Esteban et al. 2009; Rogers et al. 2021). Méndez-Delgado et al. (2023) carried out an exhaustive analysis to explain the aforementioned behaviour in the subsection 6.1 of their paper, so we do not repeat it here and only mention the most relevant results of such analysis. Those authors list the main causes that have been proposed to explain the discrepancies between T_e([N II]), T_e([O II]) and T_e([S II]), that can be classified as observational effects (incorrect flux calibration or reddening correction, telluric contamination, blends with other faint lines) or other physical reasons (mismatch between the N^+, O^+ and S^+ zones, recombination contribution to the auroral CELs, T_e fluctuations or variations in the spatial distribution of n_e inside the nebula). Méndez-Delgado et al. (2023) conclude that density inhomogeneities must certainly be the main responsible for the trends of T_e([O II]) or T_e([S II]) with respect to T_e([N II]). As shown in figure 9 of Méndez-Delgado et al. (2023), the line ratios used to determine T_e([O II]) and T_e([S II]) have a strong but very similar dependence on n_e when it is in the range from 100 to 10,000 cm^{-3} – the common density range in H II regions and SFGs in the local Universe – while those of T_e([N II]) begin to be sensitive to n_e at values above that range. In the presence of n_e inhomogeneities in a nebula, the common indicators n_e([S II]) and n_e([O II]) are biased towards the zones of lower values of n_e. Using biased density values – lower than the true ones – T_e([O II]) and T_e([S II]) would tend to be larger than T_e([N II]).

The high n_e-dependence of T_e([O II]) and T_e([S II]) indicators means that, in addition to being able to generate trends with respect to T_e([N II]), it increases the intrinsic dispersion of the T_e–T_e relations in which they are used. This effect has been discussed several times in the literature. For example, Vermeij & van der Hulst (2002) or Bresolin et al. (2009a) estimate that an uncertainty of 50–100 cm^{-3} in n_e can in turn produce uncertainties in T_e([O II]) of the order of 350–500 K, and somewhat lower in the case of T_e([S II]). Pérez-Montero & Díaz (2003), in their observed T_e([S II])–T_e([O II]) and T_e([O II])–T_e([O III]) distributions (their figures 3 and 4) introduce curves showing sequences of models computed with n_e values of 10, 100, and 500 cm^{-3}, which seem sufficient to account for their large scatter. These sequences were later used and discussed by Hägele et al. (2006, 2008) and Arellano-Córdova & Rodríguez (2020). The aforementioned effect is reflected in the large σ_{int} values of the T_e–T_e relations involving T_e indicators of the low ionisation zone shown in Table 2. Whenever T_e([O II]) or T_e([S II]) appear, the intrinsic dispersion increases, and by a similar proportion. However, all relationships involving T_e([N II]) consistently exhibit lower intrinsic dispersions. This result supports one of the conclusions of the analysis of Méndez-Delgado et al. (2023), in which it is recommended that the use of T_e([O II]) and T_e([S II]) should be avoided to calculate abundances of low-ionisation ions when T_e([N II]) is available, due to the greater reliability of the latter indicator. Unfortunately, as has been mentioned on several occasions, T_e([N II]) is very difficult to obtain at the low metallicities typical of SFGs. This is clearly reflected in Scholte et al. (2026); from almost 50,000 SFGs with z < 0.96 from the second

release of DESI data[3], they only have 340 SFGs (0.5% of the sample) with T_e([N II]) determinations.

4.2. Relations involving T_e([S III])

T_e([S III]) is the only diagnostic available in the optical spectra of star-forming regions that is commonly considered representative of the T_e of the intermediate-ionisation zone (e.g. Garnett 1992; Berg et al. 2020). The total number of selected DESIRED-E spectra with determinations of this T_e diagnostic is 345, of which 282 correspond to H II regions and 63 to SFGs. In this subsection we discuss the results for the T_e–T_e relations involving T_e([S III]) as the second element of the relation (the x-a in the graphical representations). We consider T_e([S II])–T_e([S III]), T_e([N II])–T_e([S III]), and T_e([O II])–T_e([S III]) relations, although for the latter we only provide its parameters in Table 2.

The T_e([S II])–T_e([S III]) relation has received little attention in the literature, although it may be of interest for analyzing how the temperatures of two different nebular zones compare when two ionisation states of the same element are involved. Later, in Section 4.3, we discuss the T_e([O II])–T_e([O III]) relation, which is an analogous case but has been studied much more extensively. In the top panel of Fig. 4 we represent the T_e([S II])–T_e([S III]) relation we obtain from 257 DESIRED-E spectra (216 H II regions and 41 SFGs). The ODR linear fit to the data is:

$$T_e([S\,II]) = (0.705 \pm 0.025) \times T_e([S\,III]) + (2760 \pm 210)\ K. \quad (4)$$

The correlation between the two T_e indicators is moderate-strong and statistically significant, with a Pearson coefficient of 0.63. The σ_{tot} and σ_{int} values about the linear fit to this relation for T_e([S II]) are 2090 K and 1410 K, respectively (2970 K and 2010 K for T_e([S III]), respectively). There is no published work that includes an explicit value for the slope of the T_e([S II])–T_e([S III]) relation predicted by photoionisation models. Rickards Vaught et al. (2024) present an invertible linear ODR fit to observational values of the T_e([S III])–T_e([S II]) relation for a sample of 123 extragalactic H II regions (see Fig. 4) obtaining a slope of 0.90, slightly higher than ours. On the other hand, Scholte et al. (2026) obtain 0.705 – a slope quite similar to ours – from measurements of 258 SFGs.

Unlike T_e([S II])–T_e([S III]), the T_e([N II])–T_e([S III]) relation has been widely discussed in the literature (e.g. Berg et al. 2015, 2020; Croxall et al. 2016; Rogers et al. 2021; Zurita et al. 2021; Méndez-Delgado et al. 2023; Rickards Vaught et al. 2024). In the bottom panel of Fig. 4 we represent the T_e([N II])–T_e([S III]) relation we obtain from 214 DESIRED-E spectra (204 H II regions and only 10 SFGs). The ODR linear fit to the data is:

$$T_e([N\,II]) = (0.807 \pm 0.022) \times T_e([S\,III]) + (1890 \pm 180)\ K. \quad (5)$$

Fig. 4 illustrates the remarkably tight correlation of the T_e([N II])–T_e([S III]) relation – especially for T_e([S III]) < 9000 K – with a small dispersion. In fact the values of σ_{tot} and σ_{int} of this relation for T_e([N II]) are 1240 K and 650 K, respectively – 1540 K and 800 K for T_e([S III]) –, one of the lowest σ_{int} values found in this study. The Pearson coefficient of the fit is 0.75, one of the highest values of all the T_e–T_e relations studied. Our slope of 0.807 is just between the values of 0.7 and 0.92 obtained by Garnett (1992) and Méndez-Delgado et al. (2023), respectively, from photoionisation models, and somewhat larger than the slopes obtained by Rogers et al. (2021), Zurita et al. (2021) or Rickards Vaught et al. (2024) of 0.69, 0.71, and 0.74, respectively, from observational data. All those authors – as well as Berg et al. (2015, 2020), Croxall et al. (2016) or Méndez-Delgado et al. (2023) – highlight the strong correlation and small dispersion that this relation shows. Only Scholte et al. (2026) obtain a slope significantly larger, 1.01, from data of 184 SFGs.

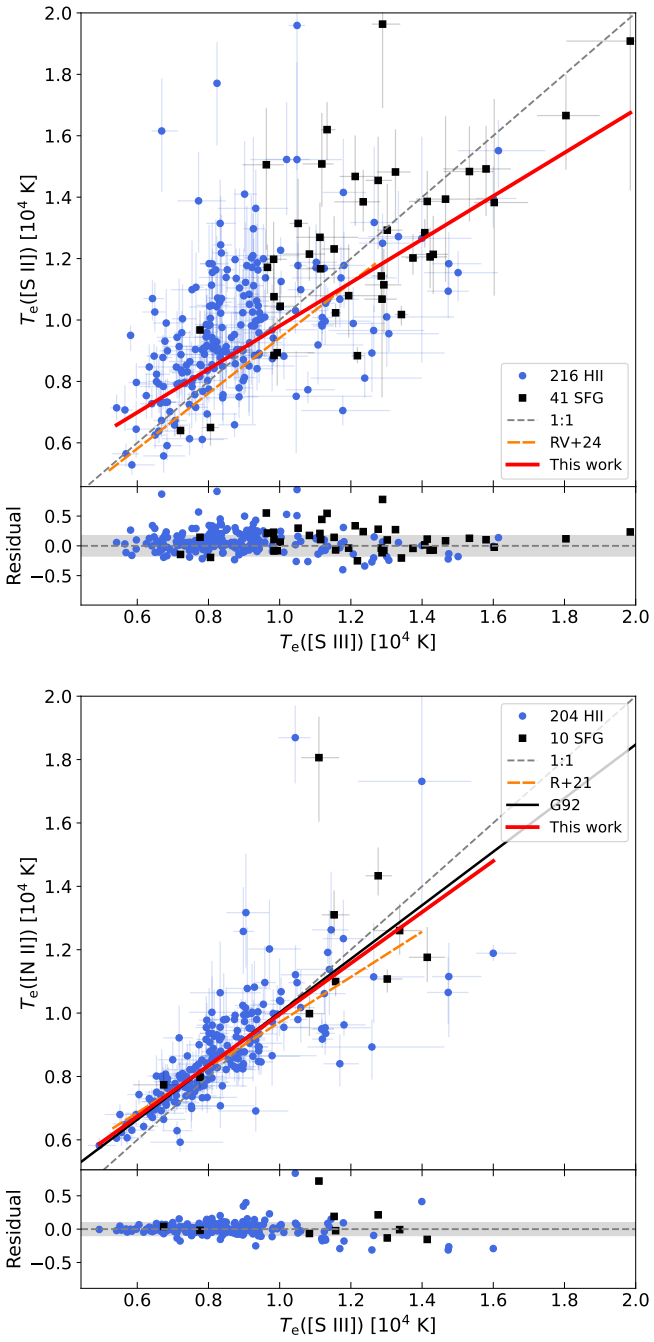


Fig. 4. T_e([S II])–T_e([S III]) (top) and T_e([N II])–T_e([S III]) (bottom) relations obtained for our DESIRED-E sample. The red continuous lines represent the ODR linear fits to the data. The grey dashed lines show the 1:1 relation. The orange dashed lines represent the linear fits to the observational data of Rickards Vaught et al. (2024) and Rogers et al. (2021) in the top and bottom panels, respectively. The black continuous line in the bottom panel represents the linear fit obtained from photoionisation models by Garnett (1992). The rectangular inset below each plot shows the residuals to the ODR linear fit, with the grey band showing the total dispersion (σ_{tot}) of the data around the fit.

[3] These data are still not public at the moment of the writing of this paper.

4.3. Relations involving T_e([O III])

Of the six T_e diagnostics we have available, T_e([O III]) is the one considered representative of the high-ionisation zone in typical star-forming regions (e.g. Garnett 1992; Berg et al. 2020). We have 498 spectra with determinations of T_e([O III]) in our sample, 315 of which are H II regions and 183 SFGs. In this subsection we discuss the results for the T_e–T_e relations involving T_e([O III]) as the second element – x-axis – of the relation, in our case T_e([O II])–T_e([O III]), T_e([N II])–T_e([O III]), T_e([S III])–T_e([O III]), and T_e([Ar III])–T_e([O III]).

In the top panel of Fig. 5 we show the T_e([O II])–T_e([O III]) relation we obtain from 380 DESIRED-E spectra, of which 258 correspond to H II regions and 122 to SFGs. The distribution of the data points shows a large dispersion and its ODR linear fit is:

$$T_e([O\,II]) = (0.523 \pm 0.017) \times T_e([O\,III]) + (5120 \pm 170)\ K. \quad (6)$$

This is the fit with the slope value furthest from unity of all the T_e–T_e relations studied. In any case, it shows a strong-moderate (r = 0.63) correlation. It is well known in the literature that the T_e([O II])–T_e([O III]) relation in H II regions exhibits a very high dispersion. Even early works such as that of Kennicutt et al. (2003) claimed that the two T_e diagnostics were uncorrelated. In our case, the σ_{tot} and σ_{int} values of this relation for T_e([O II]) are quite large, 1830 K and 1440 K, respectively, and even larger for T_e([O III]) (3500 K and 2770 K, respectively). In Section 4.1, following the conclusions of the analysis of Méndez-Delgado et al. (2023), we indicated that n_e inhomogeneities should be the main responsible for the trends and large dispersions of T_e([O II]) or T_e([S II]) with respect to other T_e indicators less sensitive to collisional de-excitation at the typical n_e values of star-forming regions. Although the spatial variations in n_e may be the most important, there are other physical phenomena that can also contribute to the larger dispersion of the T_e([O II]) diagnostic depending on the characteristics of the nebulae and the quality of the observations. The auroral [O II] $\lambda\lambda$7319 + 20 + 30 + 31 lines can be affected by recombination (dielectronic plus radiative) contribution from O^{++} ions (Rubin 1986; Liu et al. 2001). The increase in intensity of the red [O II] auroral lines due to recombination exhibits a complex and contradictory behaviour. On the one hand, it increases as the T_e decreases, and therefore as the metallicity of the object increases (Stasińska 2005). This is because recombination coefficients are larger at lower T_e. On the other hand, recombination is more significant the higher the proportion of O^{++} present, and it also depends on the degree of ionisation of the nebula, which, in turn, increases at lower metallicity. Using photoionisation models, Méndez-Delgado et al. (2023) find that the recombination contribution – if present – is clearly higher in the case of T_e([O II]) than in T_e([N II]) and that the difference between the two T_e diagnostics would be correlated with the intensity of the recombination lines of the V1 multiplet of O II, something that is not observed, although for a rather limited sample of objects due to the difficulty of measuring the extremely faint O II lines. This leads Méndez-Delgado et al. (2023) to dismiss a significant contribution of recombination to T_e([O II]) in their sample. In any case, we cannot rule out that this phenomenon could be present in a non-negligible way in some objects – especially in highly ionised ones – and thus contribute to increase the scatter of the T_e([O II]) distribution at higher T_e values.

As also discussed in Section 4.1, the calculation of T_e([O II]) is very sensitive to several observational problems that are difficult to quantify and sometimes even to identify. Several authors have detailed those observational problems that arise mainly from the large wavelength distance that separates the lines from whose ratio the T_e([O II]) diagnostic is based – [O II] $\lambda\lambda$3726 + 29 and [O II] $\lambda\lambda$7319+20+30+31 (e.g. Kennicutt et al. 2003; Rodríguez 2020; Méndez-Delgado et al. 2023). With such a long wavelength baseline, any error in flux calibration or reddening correction of the optical spectra amplifies the uncertainty of the diagnostic line ratio and hence the final T_e([O II]) error. Finally, the contamination by telluric spectral features (in emission or absorption) can affect severely the intensity of the [O II] $\lambda\lambda$7319 + 20 + 30 + 31 lines if the sky emission is not correctly corrected. This can be especially important in low resolution spectra.

Photoionisation models predict a linear T_e([O II])–T_e([O III]) relation with a slope of between 0.7 and 0.8 (Campbell et al. 1986; Garnett 1992; Deharveng et al. 2000), although some authors provide a non-linear fit between both diagnostics but with a slight curvature (Pagel et al. 1992; Thuan et al. 1995; Izotov et al. 1997, 2006). Linear fits to observational data from star-forming regions available in the literature give quite different values of the slope, although always less than or close to unity. Pilyugin et al. (2006, 2009) give values of 0.72 and 0.84, respectively, Esteban et al. (2009) obtain 0.99, Zurita et al. (2021) 0.63, and Cataldi et al. (2025), who uses a very extensive compilation of data from H II regions and SFGs – they do not indicate the total number of objects – find a slope of 0.54. One striking aspect of Cataldi et al. (2025) work is that they use the collision strengths of Palay et al. (2012) for O^{++} and, therefore, for the calculation of T_e([O III]) in their objects. This is a surprising choice because several authors have indicated that those data may not be entirely correct (Storey et al. 2014; Juan de Dios & Rodríguez 2017; Morisset et al. 2020). In fact, the collision strengths of Palay et al. (2012) give T_e([O III]) values several hundred K lower than all other available atomic data sets[4]. Finally, Scholte et al. (2026) present the linear fit of the T_e([O II])–T_e([O III]) relation with the largest number of objects: 10124 SFGs, obtaining a slope of 0.648.

In the bottom panel of Fig. 5 we show the T_e([N II])–T_e([O III]) relation for 204 DESIRED-E spectra (185 H II regions and 19 SFGs). The distribution of the data points shows a considerably smaller dispersion around the linear fit than the T_e([O II])–T_e([O III]) relation. Their ODR linear fit is:

$$T_e([N\,II]) = (0.763 \pm 0.032) \times T_e([O\,III]) + (2530 \pm 280)\ K. \quad (7)$$

The value of the Pearson coefficient of the linear fit is 0.70, which indicates a moderate-strong correlation. For T_e([N II]), the total and intrinsic dispersions about the linear fit for this T_e–T_e relation are 1360 K and 790 K, respectively, significantly lower than those of T_e([O II])–T_e([O III]) and T_e([S II])–T_e([O III]) relations, most likely due to the lower dependence of T_e([N II]) on n_e, as discussed above and in the previous subsection. For T_e([O II]), the scatter is larger, with total and intrinsic dispersions of 1780 K and 1040 K, respectively. Photoionisation models tend to obtain that T_e([O II]) $\approx$ T_e([N II]) (Campbell et al. 1986; Garnett 1992; Pagel et al. 1992; Thuan et al. 1995; Izotov et al. 1997). In this sense, the slope of 0.7 that Campbell et al. (1986) and Garnett (1992) proposed for the T_e([O II])–T_e([O III]) relation would also be applicable for the T_e([N II])–T_e([O III]) one, so our linear fit based on observations is very consistent with what is predicted by the models. However, the slope of 1.1 obtained by

[4] Morisset et al. (2020) say, quoting Storey et al. (2014), that the [O III] λ4363/λ5007 line intensity ratio that is used to derive T_e([O III]) is about 25% higher and that it is caused by Palay et al. (2012) neglecting the $2p^4kl$ free channels in the close-coupling expansion of the ion-electron system, that leads to an energy downshift of the broad $2p^5$ resonance.

Scholte et al. (2026) for this T_e–T_e relation from data of 106 SFGs is larger than our value and that expected by photonization models.

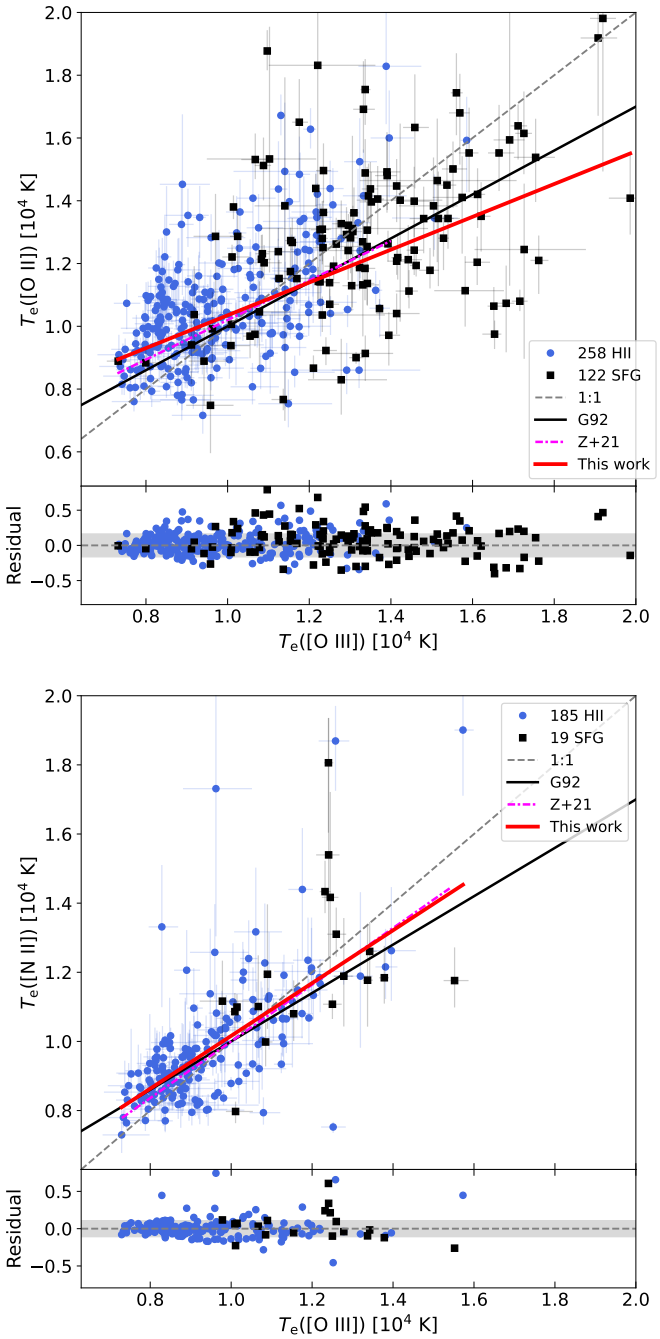


Fig. 5. T_e([O II])–T_e([O III]) (top) and T_e([N II])–T_e([O III]) (bottom) relations obtained for our DESIRED-E sample. The red continuous lines represent the ODR linear fits to the data. The grey dashed lines show the 1:1 relation. The magenta dotted-dashed lines represent the linear fits to the observational data of Zurita et al. (2021). The black continuous lines represent the linear fits obtained from photoionisation models by Garnett (1992). The rectangular inset below each plot shows the residuals to the ODR linear fit, with the grey band showing the total dispersion (σ_{tot}) of the data around the fit.

As it is illustrated in the top panel of Fig. 6, the T_e([S III])–T_e([O III]) relation defined by the DESIRED-E spectra is also fairly tight. The ODR linear fit to the 224 data points (163 H II regions and 61 SFGs) is:

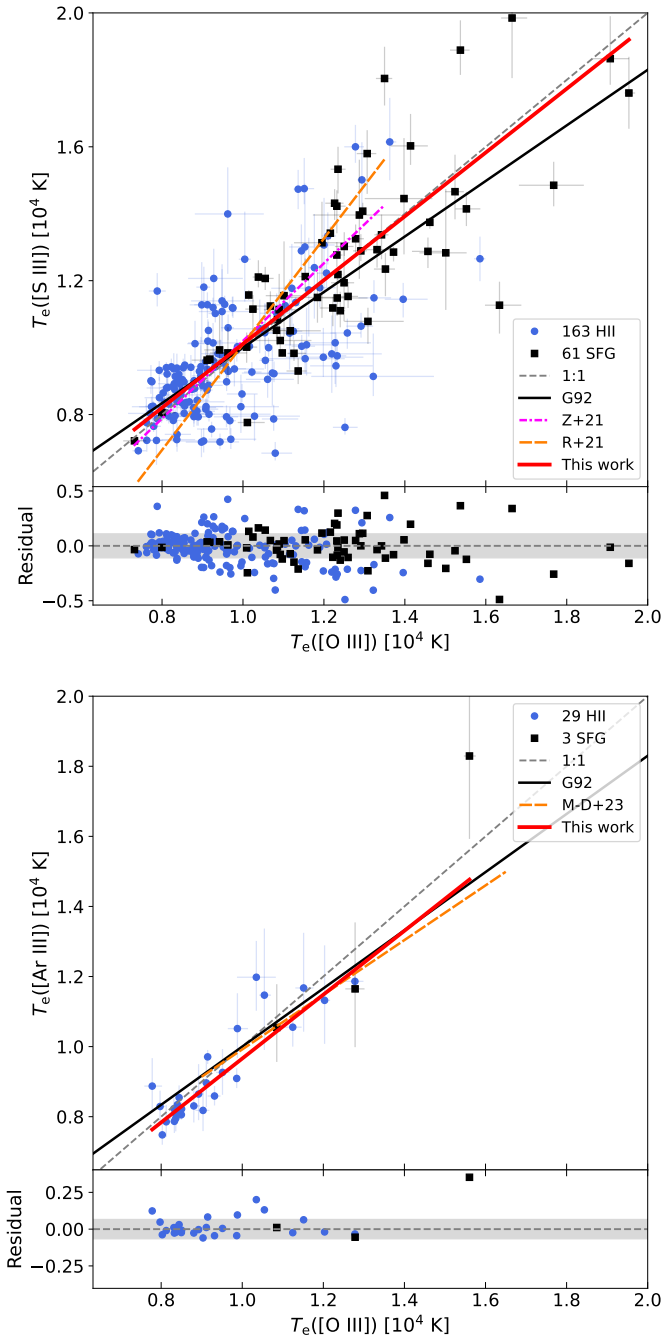


Fig. 6. T_e([S III])–T_e([O III]) (top) and T_e([Ar III])–T_e([O III]) (bottom) relations obtained for our DESIRED-E sample. The red continuous lines represent the ODR linear fits to the data. The grey dashed lines show the 1:1 relation. The black continuous lines represent the linear fits obtained from photoionisation models by Garnett (1992). In the upper panel, the orange dashed line represent the linear fits to the observational data of Rogers et al. (2021), while in the bottom panel represents de linear fit obtained from BOND models (Vale Asari et al. 2016) by Méndez-Delgado et al. (2023). The rectangular inset below each plot shows the residuals to the ODR linear fit, with the grey band showing the total dispersion (σ_{tot}) of the data around the fit.

$$T_e([\mathrm{S\,III}]) = (0.953 \pm 0.015) \times T_e([\mathrm{O\,III}]) + (580 \pm 150)\ \mathrm{K}. \quad (8)$$

The Pearson coefficient of the fit is 0.79, indicating a quite strong correlation between T_e([S III]) and T_e([O III]). The total

and the intrinsic dispersions of this relation for T_e([S III]) are quite large, 1510 K and 1280 K, respectively (1580 K and 1340 K for T_e([O III])). The slope of the linear fit is fairly consistent with that expected using photoionisation codes, as it was also found in other previous studies based on observational data (e.g. Kennicutt et al. 2003; Bresolin et al. 2009b; Zurita & Bresolin 2012). For example, Garnett (1992) found a value of 0.83, while Méndez-Delgado et al. (2023), making use of the BOND models (Vale Asari et al. 2016), obtained a slope of 0.95. However, the consistency with models predictions – as our results indicate – is not commonly found in previous observation-based T_e([S III])–T_e([O III]) relations. Several works found slightly higher slopes, of the order of 1.15, as is the case of Vermeij & van der Hulst (2002), Hägele et al. (2006) or Zurita et al. (2021). On the other hand, Binette et al. (2012) reported a substantially higher slope, of 1.41, based on data for a sample of 102 H II regions and SFGs published by Pérez-Montero et al. (2006) and Hägele et al. (2006). Binette et al. (2012) find that T_e([O III]) are systematically higher than the corresponding T_e([S III]) in objects with T_e([S III]) lower than 14,000 K. A behaviour that is not confirmed in our data. Finally, the various works of the CHAOS project that analyze the T_e([S III])–T_e([O III]) relation in H II regions of different spiral galaxies find slopes between 1.27 and 1.80 and rather high intrinsic dispersions, mainly introduced by their T_e([O III]) determinations (e.g. Croxall et al. 2016; Berg et al. 2020; Rogers et al. 2021). Finally, Scholte et al. (2026), using a large sample of 3781 SFGs, find a slope of 1.062, a value not very different from ours.

T_e([Ar III])–T_e([O III]) is the last T_e–T_e relation we discuss in this paper, which we show in the bottom panel of Fig. 6. It is the one that includes the fewest observational points (32 DESIRED-E spectra, of which 29 are H II regions and 3 SFGs) due to the extreme weakness of the auroral [Ar III] λ5192 line. The ODR fit to these T_e values is:

$$T_e([\mathrm{Ar\,III}]) = (0.911 \pm 0.069) \times T_e([\mathrm{O\,III}]) + (540 \pm 610)\ \mathrm{K}. \quad (9)$$

The relation between both T_e indicators is very tight, with a Pearson coefficient of 0.93, the highest of all the relations studied in this work. Furthermore, the total and intrinsic dispersions of this relation are the lowest we obtain, 890 K and 160 K, respectively, indicating that most of the dispersion comes from the observational errors. Photoionisation models predict a relation between T_e([Ar III]) and T_e([O III]) close to the 1:1 relation; Garnett (1992) gives a slope of 0.83 and Méndez-Delgado et al. (2023) obtain 0.95, consistent with our slope obtained from the observational data compiled in DESIRED-E. The only previous study that studied T_e–T_e relations involving observational determinations of T_e([Ar III]) is that of Méndez-Delgado et al. (2023), which included results for 17 H II regions and SFGs of the original DESIRED sample, obtaining a slope consistent with ours within the errors.

5. The application of T_e–T_e relations

As it has been commented in Sect. 1, most of the works dedicated to determining the abundances of ionised gas in star-forming regions use a two-zone (or even a three-zone in some cases) approach, but in many cases, there is only one T_e indicator for a single ionisation zone. Therefore, we have to apply a T_e–T_e relation to estimate a representative T_e of the ionisation zone for which we lack a measured indicator. In SFGs, with generally subsolar metallicities, the most common situation is to only have T_e([O III]). In H II regions in environments with metallicity close to solar, T_e([O III]) is also very common as the only available T_e indicator, although T_e([N II]) may also be well-measured, as is the case of Galactic H II regions (e.g. Arellano-Córdova et al. 2020, 2021) or those of the nearest spiral galaxies studied in the CHAOS project (e.g. Berg et al. 2015, 2020; Croxall et al. 2016; Rogers et al. 2021, 2022). When the available spectra include the reddest part of the optical range, between 7000 and 10,000 Å, it is possible to determine T_e([O II]) and/or T_e([S III]). These indicators are easier to obtain than T_e([N II]) because the [O II] $\lambda\lambda$7319, 7320, 7330, 7331 and [S III] λ6312 auroral lines are commonly brighter than [N II] λ5755. On the other hand, the [S II] $\lambda\lambda$4069, 4076 auroral lines are generally rather faint – with an intensity similar to [N II] λ5755 – but are in the blue part of the optical spectrum, where detectors are commonly less efficient and the line intensities more attenuated by dust extinction. Even so, the number of objects we have in DESIRED-E with measurements of T_e([S II]) is quite high, as we indicated in the first paragraph of Sect. 4.1. Another situation in which we have to apply T_e–T_e relations is when our instrument does not cover a part of the optical spectral range, as is the case, for example, with MUSE on the VLT, where we cannot observe lines below 4650 Å, which prevents us from obtaining T_e([O III]), T_e([O II]) and T_e([S II]) in local star-forming regions. Therefore, direct abundance determinations obtained with MUSE can only be based on T_e([S III]) and/or T_e([N II]) for those objects (e.g. Groves et al. 2023; Brazzini et al. 2024; Rickards Vaught et al. 2024).

As discussed throughout Sect. 4, some of the studied T_e–T_e relations allign more closely with photoionisation models predictions than others. In the case of relations involving T_e indicators of the low ionisation zone: T_e([O II]), T_e([N II]), and T_e([S II]), we find that the T_e([S II])–T_e([O II]) relation has a slope fairly consistent with the one predicted by photoionisation models, although with a constant offset, in the sense that T_e([O II]) is systematically on the order of 400 K larger than T_e([S II]). However, the linear fits to our observational T_e([O II])–T_e([N II]) and T_e([S II])–T_e([N II]) relations give very similar slopes and deviate in a similar way from the relation predicted by photoionisation models. The general trend is that T_e([O II]) and T_e([S II]) tend to be larger than T_e([N II]) as T_e([N II]) increases, although it shows a change in behaviour at T_e([N II]) > 12,000 K, which can be clearly seen in the residual insets of the T_e–T_e relations shown in Fig. 2. In these insets, the residuals of the ODR linear fits to the T_e([O II])–T_e([N II]) and T_e([S II])–T_e([N II]) distributions are systematically negative for T_e([N II]) > 12,000 K.

However, the number of objects with available T_e([N II]) determinations at such high T_e values is very limited and could be affected by observational bias. In fact, objects with higher T_e tend to have lower metallicity and a higher ionisation degree, so the amount of N^+ is very small and, therefore, their [N II] λ5755/Hβ intensity ratio very small. This means that the value of T_e([N II]) of our observational points tends to be correlated with its error. Moreover, it is even possible that the intensity of [N II] λ5755 may have been overestimated in some high-T_e objects (e.g. Rola & Pelat 1994). On the other hand, inspecting Table 2, we can see how the T_e–T_e relations involving T_e([N II]) consistently show σ_{int} values on the order of a factor of two less to those involving T_e([O II]) or T_e([S II]). Considering the discussion outlined in Sect. 4.1, the results described in this paragraph can be explained by the different dependence of T_e([O II]), T_e([S II]), and T_e([N II]) on n_e and the presence of n_e inhomogeneities in the ionised gas. The possible effects of the degree of ionization are discussed briefly in Appendix C.

As a first recommendation, we propose that when T_e([O III]) and/or T_e([S III]) are available, but not a low-ionisation zone indicator, the best option is to use the T_e([N II])–T_e([O III]) and/or

T_e([N II])–T_e([S III]) relations to obtain T_e([N II]). This choice guarantees an assumed T_e value with less intrinsic error for the low-ionisation zone. Photoionisation models agree that T_e([O II]) ≈ T_e([N II]) (Campbell et al. 1986; Garnett 1992; Thuan et al. 1995; Izotov et al. 1997), so using T_e([N II]) for calculating the abundance of low-ionisation ions, especially the O^+/H^+ ratio, seems a more than reasonable approximation. In any case, it should be noted that, because the number of determinations is very small at high T_e([N II]) values, the T_e([N II])–T_e([S III]) relation can be considered valid for T_e([S III]) < 16,000 K and the T_e([N II])–T_e([O III]) relation for T_e([O III]) < 14,000 K; above those values the relations should be considered quite unreliable. As discussed in Sect. 4.2 and 4.3, our linear ODR fits to the T_e([N II])–T_e([S III]), T_e([O II])–T_e([S III]), T_e([N II])–T_e([O III]), and T_e([Ar III])–T_e([O III]) distributions are fairly consistent with the predictions of photoionisation models (e.g. Garnett 1992; Méndez-Delgado et al. 2023), while the fits to the T_e([O II])–T_e([O III]) and T_e([S III])–T_e([O III]) ones do not show such a good consistency, but a reasonable one in any case. It is worth noting that the degree of consistency with the photoionisation models tends to increase with decreasing values of the σ_{int} of the ODR linear fit.

6. Conclusions

In this work we have carried out a homogeneous analysis of T_e derived from six optical CEL diagnostics – T_e([N II]), T_e([O II]), T_e([S II]), T_e([S III]), T_e([O III]), and T_e([Ar III]) – using 699 spectra of Galactic and extragalactic H II regions and star-forming galaxies compiled in the DESIRED-E database. We recomputed n_e and T_e with updated atomic data and a consistent methodology, allowing us to explore the behaviour of the different T_e–T_e relations. Our main results can be summarised as follows:

1. Relations involving low-ionisation diagnostics exhibit significant large σ_{int} values. In particular, the relations involving the T_e([O II]) and T_e([S II]) diagnostics show the largest dispersions, which can be explained by their stronger sensitivity to n_e inhomogeneities, possible recombination contributions, and observational uncertainties related to the large wavelength baselines involved on these diagnostics.
2. T_e–T_e relations with T_e([N II]) in the y-axis give σ_{int} values consistently lower than the equivalent relations involving T_e([O II]) or T_e([S II]). This may be due to the lower n_e-sensitivity of this T_e diagnostic. We recommend using relations involving T_e([N II]) instead of T_e([O II]) or T_e([S II]) to estimate a representative T_e of the low-ionisation zone when only T_e([O III]) and/or T_e([S III]) are available, due to the apparent greater reliability of T_e([N II]). Unfortunately, T_e([N II]) can be extremely faint and very difficult to detect at the low metallicities typical of SFGs.
3. Among the relations involving intermediate- and high-ionisation diagnostics, T_e([Ar III])–T_e([O III]) shows the tightest relation obtained in this study, although the number of available measurements of the auroral [Ar III] λ5192 line is very limited.
4. The slopes of the ODR linear fits applied to the T_e–T_e relations are broadly consistent with those predicted by photoionisation models, especially in the cases of T_e([N II])–T_e([S III]), T_e([O II])–T_e([S III]), T_e([N II])–T_e([O III]), and T_e([Ar III])–T_e([O III]) relations. The degree of agreement improves for relations with lower σ_{int}, suggesting that physical and observational limitations dominate the discrepancies.
5. The set of empirical T_e–T_e relations presented here provides a homogeneous observational foundation for estimating T_e in objects where only one diagnostic is available. These relations are particularly valuable for the determination of chemical abundances in local extragalactic H II regions – our sample is significantly much more limited for SFGs and, in principle, less applicable for these objects –, where T_e([O III]) is often the only T_e diagnostic available.

Overall, this study provides the most comprehensive observational characterisation to date of the relationships among the different T_e diagnostics in local H II regions. As the DESIRED-E database continues to expand, future work combining these data with deep spatially resolved spectroscopy of star-forming regions will enable an increasingly refined view of the T_e structure in ionised regions of the local Universe.

Data Availability

The complete tables of references, physical conditions and chemical abundances for all the objects in our sample can be found at: https://zenodo.org/records/19471717.

Acknowledgements. MOG, CE, JGR and ERR acknowledge financial support from the Agencia Estatal de Investigación of the Ministerio de Ciencia e Innovación y Universidades (AEI-MCIU) under grant "The internal structure of ionised nebulae and its effects in the determination of the chemical composition of the interstellar medium and the Universe" with reference PID2023-151648NB-I00 (DOI:10.13039/5011000110339). JGR also acknowledges support from the AEI-MCIU and from the European Regional Development Fund (ERDF) under grant "Planetary nebulae as the key to understanding binary stellar evolution" with reference PID2022-136653NA-I00 (DOI:10.13039/501100011033). AZLA gratefully acknowledges the support provided by the Postdoctoral Program (POSDOC) of UNAM (Universidad Nacional Autónoma de México). JEMD and AZLA also acknowledge support from the SECIHTI project CBF-2025-I-2048, "Resolviendo la Física Interna de las Galaxias: De las Escalas Locales a la Estructura Global con el SDSS-V Local Volume Mapper". JEMD, MOG, CE, JGR, AZLA, KZAC, FFRO and ERR thank the support by UNAM/DGAPA/PAPIIT/IA103326 project "DESIRED (DEep Spectra of ionised Regions Database): de las emisiones más sutiles a la física fundamental del universo" .

References

Aller, L. H., Hung, S., & Feibelman, W. A. 1999, Proceedings of the National Academy of Science, 96, 5366
Arellano-Córdova, K. Z., Berg, D. A., Chisholm, J., et al. 2022, ApJ, 940, L23
Arellano-Córdova, K. Z., Cullen, F., Carnall, A. C., et al. 2025, MNRAS, 540, 2991
Arellano-Córdova, K. Z., Esteban, C., García-Rojas, J., & Méndez-Delgado, J. E. 2020, MNRAS, 496, 1051
Arellano-Córdova, K. Z., Esteban, C., García-Rojas, J., & Méndez-Delgado, J. E. 2021, MNRAS, 502, 225
Arellano-Córdova, K. Z. & Rodríguez, M. 2020, MNRAS, 497, 672
Baldwin, J. A., Phillips, M. M., & Terlevich, R. 1981, PASP, 93, 5
Berg, D. A., Pogge, R. W., Skillman, E. D., et al. 2020, ApJ, 893, 96
Berg, D. A., Skillman, E. D., Croxall, K. V., et al. 2015, ApJ, 806, 16
Berg, D. A., Skillman, E. D., Garnett, D. R., et al. 2013, ApJ, 775, 128
Binette, L., Matadamas, R., Hägele, G. F., et al. 2012, A&A, 547, A29
Brazzini, M., Belfiore, F., Ginolfi, M., et al. 2024, A&A, 691, A173
Bresolin, F. 2007, ApJ, 656, 186
Bresolin, F., Gieren, W., Kudritzki, R.-P., et al. 2009a, ApJ, 700, 309
Bresolin, F., Ryan-Weber, E., Kennicutt, R. C., & Goddard, Q. 2009b, ApJ, 695, 580
Butler, K. & Zeippen, C. J. 1989, A&A, 208, 337
Campbell, A., Terlevich, R., & Melnick, J. 1986, MNRAS, 223, 811
Cataldi, E., Belfiore, F., Curti, M., et al. 2025, arXiv e-prints, arXiv:2504.03839
Croxall, K. V., Pogge, R. W., Berg, D. A., Skillman, E. D., & Moustakas, J. 2016, ApJ, 830, 4
Curti, M., D'Eugenio, F., Carniani, S., et al. 2023, MNRAS, 518, 425
Deb, N. C. & Hibbert, A. 2009, Atomic Data and Nuclear Data Tables, 95, 184
Deharveng, L., Peña, M., Caplan, J., & Costero, R. 2000, MNRAS, 311, 329

Delgado-Inglada, G., Mesa-Delgado, A., García-Rojas, J., Rodríguez, M., & Esteban, C. 2016, MNRAS, 456, 3855
Dinerstein, H. L. 1990, in Astrophysics and Space Science Library, Vol. 161, The Interstellar Medium in Galaxies, ed. J. Thronson, Harley A. & J. M. Shull, 257–285
Domínguez-Guzmán, G., Rodríguez, M., García-Rojas, J., Esteban, C., & Toribio San Cipriano, L. 2022, MNRAS, 517, 4497
Esteban, C., Bresolin, F., García-Rojas, J., & Toribio San Cipriano, L. 2020, MNRAS, 491, 2137
Esteban, C., Bresolin, F., Peimbert, M., et al. 2009, ApJ, 700, 654
Esteban, C., Carigi, L., Copetti, M. V. F., et al. 2013, MNRAS, 433, 382
Esteban, C., Fang, X., García-Rojas, J., & Toribio San Cipriano, L. 2017, MNRAS, 471, 987
Esteban, C. & García-Rojas, J. 2018, MNRAS, 478, 2315
Esteban, C., García-Rojas, J., Carigi, L., et al. 2014, MNRAS, 443, 624
Esteban, C., Peimbert, M., García-Rojas, J., et al. 2004, MNRAS, 355, 229
Fernández, V., Amorín, R., Pérez-Montero, E., et al. 2022, MNRAS, 511, 2515
Fernández, V., Terlevich, E., Díaz, A. I., Terlevich, R., & Rosales-Ortega, F. F. 2018, MNRAS, 478, 5301
Fernández-Martín, A., Pérez-Montero, E., Vílchez, J. M., & Mampaso, A. 2017, A&A, 597, A84
Fritzsche, S., Fricke, B., Geschke, D., Heitmann, A., & Sienkiewicz, J. E. 1999, ApJ, 518, 994
Froese Fischer, C. & Tachiev, G. 2004a, Atomic Data and Nuclear Data Tables, 87, 1
Froese Fischer, C. & Tachiev, G. 2004b, Atomic Data and Nuclear Data Tables, 87, 1
Froese Fischer, C., Tachiev, G., & Irimia, A. 2006, Atomic Data and Nuclear Data Tables, 92, 607
Galavis, M. E., Mendoza, C., & Zeippen, C. J. 1995, A&AS, 111, 347
García-Rojas, J., Esteban, C., Peimbert, A., et al. 2005, MNRAS, 362, 301
García-Rojas, J., Esteban, C., Peimbert, A., et al. 2007, Rev. Mexicana Astron. Astrofis., 43, 3
García-Rojas, J., Esteban, C., Peimbert, M., et al. 2006, MNRAS, 368, 253
García-Rojas, J., Esteban, C., Peimbert, M., et al. 2004, ApJS, 153, 501
Garnett, D. R. 1992, AJ, 103, 1330
Grieve, M. F. R., Ramsbottom, C. A., Hudson, C. E., & Keenan, F. P. 2014, ApJ, 780, 110
Groves, B., Kreckel, K., Santoro, F., et al. 2023, MNRAS, 520, 4902
Guseva, N. G., Izotov, Y. I., Stasińska, G., et al. 2011, A&A, 529, A149
Guseva, N. G., Izotov, Y. I., & Thuan, T. X. 2000, ApJ, 531, 776
Guseva, N. G., Papaderos, P., Izotov, Y. I., et al. 2003, A&A, 407, 105
Guseva, N. G., Papaderos, P., Meyer, H. T., Izotov, Y. I., & Fricke, K. J. 2009, A&A, 505, 63
Guseva, N. G., Thuan, T. X., & Izotov, Y. I. 2024, MNRAS, 527, 3932
Hägele, G. F., Díaz, Á. I., Terlevich, E., et al. 2008, MNRAS, 383, 209
Hägele, G. F., Pérez-Montero, E., Díaz, Á. I., Terlevich, E., & Terlevich, R. 2006, MNRAS, 372, 293
Hogg, D. W., Bovy, J., & Lang, D. 2010, arXiv e-prints, arXiv:1008.4686
Irimia, A. & Froese Fischer, C. 2005, Phys. Scr, 71, 172
Izotov, Y. I., Guseva, N. G., Fricke, K. J., & Papaderos, P. 2009, A&A, 503, 61
Izotov, Y. I., Papaderos, P., Guseva, N. G., Fricke, K. J., & Thuan, T. X. 2004, A&A, 421, 539
Izotov, Y. I., Stasińska, G., Meynet, G., Guseva, N. G., & Thuan, T. X. 2006, A&A, 448, 955
Izotov, Y. I. & Thuan, T. X. 2004, ApJ, 602, 200
Izotov, Y. I., Thuan, T. X., & Guseva, N. G. 2017, MNRAS, 471, 548
Izotov, Y. I., Thuan, T. X., & Guseva, N. G. 2021, MNRAS, 508, 2556
Izotov, Y. I., Thuan, T. X., & Lipovetsky, V. A. 1994, ApJ, 435, 647
Izotov, Y. I., Thuan, T. X., & Lipovetsky, V. A. 1997, ApJS, 108, 1
Izotov, Y. I., Thuan, T. X., & Stasińska, G. 2007, ApJ, 662, 15
Juan de Dios, L. & Rodríguez, M. 2017, MNRAS, 469, 1036
Kauffmann, G., Heckman, T. M., Tremonti, C., et al. 2003, MNRAS, 346, 1055
Kaufman, V. & Sugar, J. 1986, Journal of Physical and Chemical Reference Data, 15, 321
Kennicutt, Robert C., J., Bresolin, F., & Garnett, D. R. 2003, ApJ, 591, 801
Kewley, L. J., Dopita, M. A., Sutherland, R. S., Heisler, C. A., & Trevena, J. 2001, ApJ, 556, 121
Kisielius, R., Storey, P. J., Ferland, G. J., & Keenan, F. P. 2009, MNRAS, 397, 903
Kurt, C. M., Dufour, R. J., Garnett, D. R., et al. 1999, ApJ, 518, 246
Liu, X. W., Luo, S. G., Barlow, M. J., Danziger, I. J., & Storey, P. J. 2001, MNRAS, 327, 141
López-Sánchez, A. R. & Esteban, C. 2009, A&A, 508, 615
López-Sánchez, Á. R., Esteban, C., García-Rojas, J., Peimbert, M., & Rodríguez, M. 2007, ApJ, 656, 168
Luridiana, V., Morisset, C., & Shaw, R. A. 2015, A&A, 573, A42
Méndez-Delgado, J. E., Esteban, C., García-Rojas, J., et al. 2023, MNRAS, 523, 2952
Méndez-Delgado, J. E., Esteban, C., García-Rojas, J., & Henney, W. J. 2022, MNRAS, 514, 744
Méndez-Delgado, J. E., Esteban, C., García-Rojas, J., et al. 2021a, MNRAS, 502, 1703
Méndez-Delgado, J. E., Esteban, C., García-Rojas, J., Kreckel, K., & Peimbert, M. 2024a, Nature Astronomy, 8, 275
Méndez-Delgado, J. E., Henney, W. J., Esteban, C., et al. 2021b, ApJ, 918, 27
Méndez-Delgado, J. E., Kreckel, K., Esteban, C., et al. 2024b, A&A, 690, A248
Mendoza, C. 1983, in IAU Symposium, Vol. 103, Planetary Nebulae, ed. L. H. Aller, 143–172
Mendoza, C., Méndez-Delgado, J. E., Bautista, M., García-Rojas, J., & Morisset, C. 2023, Atoms, 11, 63
Mendoza, C. & Zeippen, C. J. 1982, MNRAS, 198, 127
Mesa-Delgado, A., Esteban, C., García-Rojas, J., et al. 2009, MNRAS, 395, 855
Morisset, C., Luridiana, V., García-Rojas, J., et al. 2020, Atoms, 8, 66
Noeske, K. G., Guseva, N. G., Fricke, K. J., et al. 2000, A&A, 361, 33
Noll, S., Kausch, W., Barden, M., et al. 2012, A&A, 543, A92
Oey, M. S., Dopita, M. A., Shields, J. C., & Smith, R. C. 2000, ApJS, 128, 511
Pagel, B. E. J., Simonson, E. A., Terlevich, R. J., & Edmunds, M. G. 1992, MNRAS, 255, 325
Palay, E., Nahar, S. N., Pradhan, A. K., & Eissner, W. 2012, MNRAS, 423, L35
Peña-Guerrero, M. A., Peimbert, A., Peimbert, M., & Ruiz, M. T. 2012, ApJ, 746, 115
Peimbert, A. 2003, ApJ, 584, 735
Peimbert, A., Peña-Guerrero, M. A., & Peimbert, M. 2012, ApJ, 753, 39
Peimbert, A., Peimbert, M., & Ruiz, M. T. 2005, ApJ, 634, 1056
Peimbert, M. & Costero, R. 1969, Boletin de los Observatorios Tonantzintla y Tacubaya, 5, 3
Peimbert, M., Pena, M., & Torres-Peimbert, S. 1986, A&A, 158, 266
Pérez-Montero, E. & Díaz, A. I. 2003, MNRAS, 346, 105
Pérez-Montero, E., Díaz, A. I., Vílchez, J. M., & Kehrig, C. 2006, A&A, 449, 193
Pilyugin, L. S., Mattsson, L., Vílchez, J. M., & Cedrés, B. 2009, MNRAS, 398, 485
Pilyugin, L. S., Vílchez, J. M., & Thuan, T. X. 2006, MNRAS, 370, 1928
Ramsbottom, C. A. & Bell, K. L. 1997, Atomic Data and Nuclear Data Tables, 66, 65
Rickards Vaught, R. J., Sandstrom, K. M., Belfiore, F., et al. 2024, ApJ, 966, 130
Rodríguez, M. 2020, MNRAS, 495, 1016
Rogers, N. S. J., Skillman, E. D., Pogge, R. W., et al. 2022, ApJ, 939, 44
Rogers, N. S. J., Skillman, E. D., Pogge, R. W., et al. 2021, ApJ, 915, 21
Rola, C. & Pelat, D. 1994, A&A, 287, 676
Rubin, R. H. 1986, ApJ, 309, 334
Rynkun, P., Gaigalas, G., & Jönsson, P. 2019, A&A, 623, A155
Schaerer, D., Marques-Chaves, R., Barrufet, L., et al. 2022, A&A, 665, L4
Scholte, D., Cullen, F., Moustakas, J. M., et al. 2026, arXiv e-prints, arXiv:2601.02463
Skillman, E. D., Côté, S., & Miller, B. W. 2003, AJ, 125, 610
Stasińska, G. 1980, A&A, 85, 359
Stasińska, G. 1982, A&AS, 48, 299
Stasińska, G. 1990, A&AS, 83, 501
Stasińska, G. 2005, A&A, 434, 507
Stasińska, G. & Schaerer, D. 1997, A&A, 322, 615
Storey, P. J. & Hummer, D. G. 1995, MNRAS, 272, 41
Storey, P. J., Sochi, T., & Badnell, N. R. 2014, MNRAS, 441, 3028
Storey, P. J. & Zeippen, C. J. 2000, MNRAS, 312, 813
Sutherland, R. S. & Dopita, M. A. 1993, ApJS, 88, 253
Tayal, S. S. 2004, A&A, 426, 717
Tayal, S. S. & Zatsarinny, O. 2010, ApJS, 188, 32
Thuan, T. X. & Izotov, Y. I. 2005, ApJS, 161, 240
Thuan, T. X., Izotov, Y. I., & Lipovetsky, V. A. 1995, ApJ, 445, 108
Toribio San Cipriano, L., García-Rojas, J., Esteban, C., Bresolin, F., & Peimbert, M. 2016, MNRAS, 458, 1866
Trump, J. R., Arrabal Haro, P., Simons, R. C., et al. 2023, ApJ, 945, 35
Vale Asari, N., Stasińska, G., Morisset, C., & Cid Fernandes, R. 2016, MNRAS, 460, 1739
Valerdi, M., Peimbert, A., & Peimbert, M. 2021, MNRAS, 505, 3624
Valerdi, M., Peimbert, A., Peimbert, M., & Sixtos, A. 2019, ApJ, 876, 98
Veilleux, S. & Osterbrock, D. E. 1987, ApJS, 63, 295
Vermeij, R. & van der Hulst, J. M. 2002, A&A, 391, 1081
Wiese, W. L., Fuhr, J. R., & Deters, T. M. 1996, Journal of Physical and Chemical Reference Data, Monograph 7, 403
Yates, R. M., Schady, P., Chen, T.-W., Schweyer, T., & Wiseman, P. 2020, A&A, 634, A107
Zhang, H. 1996, A&AS, 119, 523
Zurita, A. & Bresolin, F. 2012, MNRAS, 427, 1463
Zurita, A., Florido, E., Bresolin, F., Pérez-Montero, E., & Pérez, I. 2021, MNRAS, 500, 2359

Appendix A: References for the spectroscopic data

The complete reference tables associated with Appendix A can be found at: https://zenodo.org/records/1947177

The references for the spectroscopic data are: Arellano-Córdova et al. (2021); Berg et al. (2013); Bresolin (2007); Delgado-Inglada et al. (2016); Domínguez-Guzmán et al. (2022); Esteban et al. (2004, 2009, 2013, 2014, 2017, 2020); Esteban & García-Rojas (2018); Fernández et al. (2018, 2022); Fernández-Martín et al. (2017); García-Rojas et al. (2004, 2005, 2006, 2007); Guseva et al. (2000, 2003, 2009, 2011, 2024); Izotov et al. (1994, 1997, 2004, 2006, 2009, 2017, 2021); Izotov & Thuan (2004); Kurt et al. (1999); López-Sánchez et al. (2007); López-Sánchez & Esteban (2009); Méndez-Delgado et al. (2021a,b, 2022); Mesa-Delgado et al. (2009); Noeske et al. (2000); Peimbert et al. (1986, 2005, 2012); Peimbert (2003); Peña-Guerrero et al. (2012); Rogers et al. (2022); Skillman et al. (2003); Thuan et al. (1995); Thuan & Izotov (2005); Toribio San Cipriano et al. (2016); Valerdi et al. (2019, 2021); Zurita & Bresolin (2012)

Appendix B: Median electron temperatures for each ion and group of objects

In Fig. B.1, we show the histograms of the different T_e indicators used in this paper, T_e([N II]), T_e([O II]), T_e([S II]), T_e([S III]), T_e([O III]), and T_e([Ar III]) separated by group of objects: H II regions and SFGs. The median of the different T_e values separated by group of objects, the number of objects represented in each case, and their median value of 12+log(O/H), are included in Table B.1. From Fig. B.1 and Table B.1 it is clear that H II regions and SFGs show a quite different median value of any T_e considered, being always larger in the case of SFGs. This is mainly due to their lower median metallicity. While the representative median value of 12+log(O/H) of our sample of H II regions is around 8.41, the median drops to 8.06 in the case of SFGs. It is striking that, regardless of the number of objects – which can be very different for the different T_e indicators – the ratio between the median T_e values of SFGs and H II regions (last column of Table B.1) is significantly constant, between 1.35 and 1.45, regardless of the atom and ionisation state we consider. This indicates that all the T_e indicators exhibit a basically similar dependence on metallicity.

Other studies that compare median values of different T_e indicators in a similar way are those by Rickards Vaught et al. (2024) and Scholte et al. (2026). Rickards Vaught et al. (2024) present median values for T_e([N II]), T_e([O II]), T_e([S II]), and T_e([S III]) for a similar, though slightly smaller, number of H II regions than ours, but significantly smaller (only 26) in the case of T_e([O III]). The median values of Rickards Vaught et al. (2024) are very similar to ours for H II regions, with differences on the order of or less than 500 K for T_e([N II]), T_e([O II]), T_e([S II]), and T_e([S III]). In the case of T_e([O III]), their median value is approximately 2400 K higher than ours, deviating much further from the values of the other T_e indicators. Rickards Vaught et al. (2024) ordering of the median values from lowest to highest is: T_e([N II]), T_e([S III]), T_e([S II]), T_e([O II]), and T_e([O III]), quite similar to the one we found, except that the order of the two lowest values is swapped: T_e([S III]), T_e([N II]), T_e([S II]), T_e([O II]), and T_e([O III]) in our determinations. Scholte et al. (2026) also obtain median values for T_e([N II]), T_e([O II]), T_e([S II]), T_e([S III]), and T_e([O III]), but for a much larger number of SFGs than we do, especially for T_e([O II]), T_e([S III]), and T_e([O III]), so their results, in principle, should be statistically more significant for these objects and T_e indicators. Most median T_e values we obtain for our more limited sample of SFGs are quite different from those of Scholte et al. (2026). While our median of T_e([S III]) is identical, the ones of T_e([N II]) and T_e([O III]) are around 1000 K lower than the medians obtained by Scholte et al. (2026). In the case of T_e([O II]) and T_e([S II]), our medians are around 2500 K higher. This large difference is difficult to explain and cannot be attributed to the atomic data used. In the case of O^+, they are exactly the same, while for S^+ they differ in the transition probability reference – Scholte et al. (2026) use Rynkun et al. (2019) –, although the use of one or the other can not account for the large difference between the median value of T_e([S II]) reported in both works[5]. The difference also does not appear to be necessarily related to the very different number of objects used to obtain the values for each indicator. For example, the contrast is not so pronounced in the case of T_e([S II]). While we counted T_e([S II]) determinations for 126 SFGs, the sample for Scholte et al. (2026) is 421, but the difference between the median values is about 2400 K, which indicates that there should be a significant systematic effect on T_e([S II]) determination between the two studies. There is another important disparity between our set of median T_e values for SFGs and those reported by Scholte et al. (2026). In our case, the maximum discrepancy among the different temperature indicators does not exceed 1300 K, whereas in the calculations of Scholte et al. (2026) the corresponding differences reach approximately 3700 K. All temperature indicators associated with the low-ionisation zone in Scholte et al. (2026) data, namely T_e([N II]), T_e([O II]), and T_e([S II]), yield median values close to 10,500 K, while T_e([O III]) shows a significantly higher median temperature of about 14,000 K. These large disparities are difficult to understand, mainly because they do not appear to be due to a simple metallicity effect. Certainly, no major differences in metallicity would be expected between the SFG subsamples used by Scholte et al. (2026) to obtain their values for each T_e indicator.

Appendix C: Residuals as a Function of the ionisation Degree

In this Appendix we explore the possible impact of the ionisation conditions on the temperature relations analysed throughout this work. Fig. C.1 shows the residuals, derived as $T_y - (m \times T_x + n)$, as a function of the temperature on which the relation is based. The relations shown are T_e([O II]) and T_e([S III]) as functions of T_e([O III]) (left and central panels of Fig. C.1, respectively), and T_e([N II]) as a function of T_e([S III]) (right panel of Fig. C.1). The data points are color-coded according to their ionisation degree.

The ionisation degree is used here as a proxy for the ionisation parameter, allowing us to assess whether variations in the radiation field may introduce systematic effects in the derived temperature relations. If the ionisation parameter were a dominant factor, one would expect to observe a trend in the residuals as a function of the color scale. The diagrams show that the dispersion of the residuals increases towards higher electron temperatures. This behaviour is consistent with the fact that higher temperatures are typically associated with regions of higher excitation and, therefore, higher ionisation degree. However, despite this increase in scatter, no clear systematic dependence of the residuals on the ionisation degree is observed at fixed temperature.

[5] The use of the transition probabilities of Rynkun et al. (2019) provide values about 200 K lower than those of Irimia & Froese Fischer (2005) when T_e([S II])~10,000 K. The difference increases at higher temperatures, being about 800 K lower when T_e([S II])~18,000 K

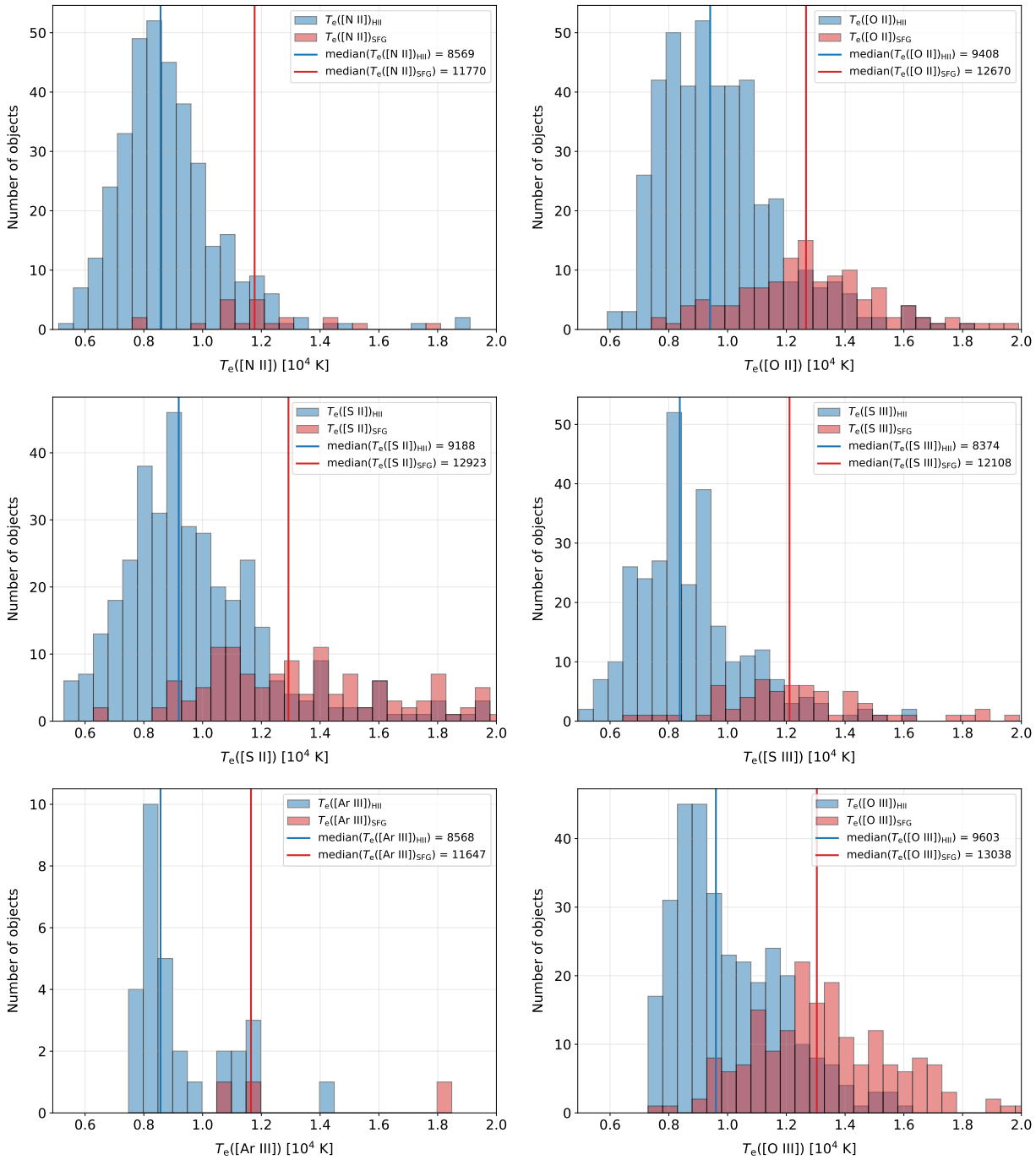


Fig. B.1. Histograms of the different T_e indicators used in this paper separated by group of objects: H II regions (blue bars) and SFGs (red bars). We use 500 K wide bins. The blue and red vertical lines show the median T_e values for H II regions and SFGs, respectively. The number of objects represented in each diagram and the median values of T_e and 12+log(O/H) are given in Table B.1

In particular, the residuals do not display any monotonic trend with the ionisation parameter, nor do they show a segregation that would indicate a secondary dependence of the temperature relations on this quantity. The distribution of points remains broadly symmetric around zero across the full range of ionisation conditions. These results indicate that, although the ionisation degree is somehow correlated with temperature and contributes to the overall increase in dispersion at the high-temperature end, it does not appear to be the primary driver of the deviations from the fitted relations.

Table B.1. Median of the different T_e indicators and group of objects

	H II regions			SFGs			
T_e	Median T_e	No.	Median 12+log(O/H)	Median T_e	No.	Median 12+log(O/H)	T_e ratio SFGs/H II
T_e([N II])	8569	350	8.45	11770	21	8.07	1.37
T_e([O II])	9408	435	8.41	12670	123	8.04	1.35
T_e([S II])	9188	361	8.41	12923	126	8.05	1.41
T_e([S III])	8374	282	8.43	12108	63	8.09	1.45
T_e([Ar III])	8568	29	8.45	11647	3	8.07	1.36
T_e([O III])	9603	315	8.32	13038	183	8.05	1.36

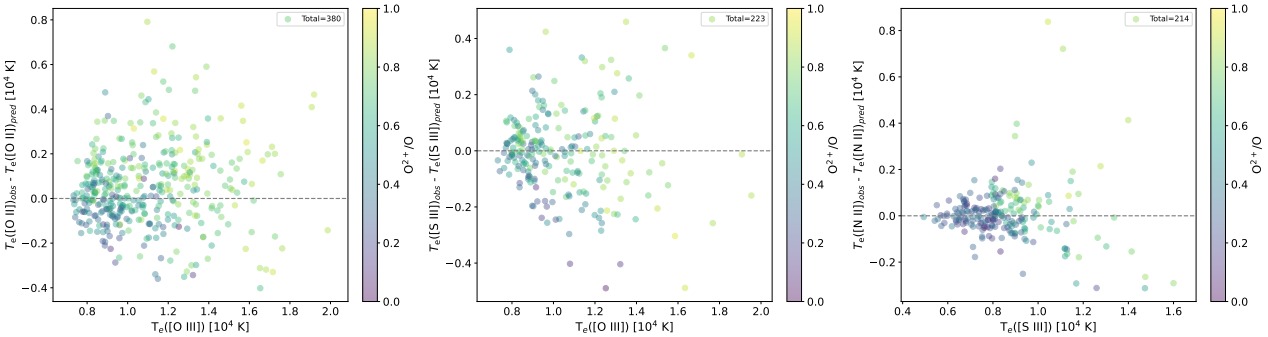


Fig. C.1. Residuals of the temperature relations as a function of the diagnostic in which the relation is based: T_e([O II])-T_e([O III]) (left), T_e([S III])-T_e([O III]) (center) and T_e([N II])-T_e([S III]) (right). The residuals are defined as the difference between the observed temperature and the one predicted by the corresponding relation. The color of the points varies according to their ionisation degree.